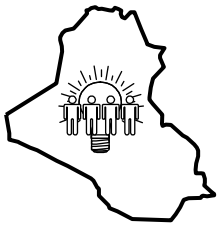

SPONSORED AND PUBLISHED BY
THE IRAQI SOCIETY FOR ALTERNATIVE AND RENEWABLE ENERGY SOURCES AND TECHNIQUES (I.S.A.R.E.S.T.)

EDITORIAL BOARD

ADVISORY BOARD

 ISSN 1813-2065 Printed in IRAQ

Organized by I.S.A.R.E.S.T.

INVITATION TO PARTICIPATE

WHAT IS ENERGY?

Energy is neither created nor destroyed. This is called the principle of Conservation of Energy. In other words, the amount of energy in the universe always remains the same. And when we use energy, like burning wood to generate light and heat, we don't use it up; we simply transform it from one form of potential energy (fuel) into other forms of kinetic energy (heat and light).
Almost all energy transformations involve the production of heat, which is considered the lowest form of energy, because it quickly dissipates into the surroundings and is normally unavailable for further use. So, although the total amount of energy remains the same, the amount of "useable" energy constantly decreases. However, don't worry too much about the decrease of useable energy; our Sun is scheduled to produce solar energy for many years to come, so taking this course will not be a waste of your time (or energy).
Energy is all around us. It heats our homes, powers our light bulbs and appliances, fuels our cars and provides for a variety of professional careers that deal with its many elements. It also comes in many forms such as heat, light, chemical, mechanical and electrical energy. And, according to physicists, energy can neither be created nor destroyed, only converted from one form to another. So why learn about energy? The answer is because energy, and the conversion of energy from one form to another, is fundamental to our modern living environment. By knowing the principles behind energy generation and conversion, you will come away with a knowledge base that can be applied to nearly every modern electrical, mechanical and chemical device that uses or produces power.
To introduce more about the alternative and renewable energy sources and techniques, I.S.A.R.E.S.T. invites you to attend the scientific lectures organized by I.S.A.R.E.S.T. You are requested to contact the secretary of the society and register your attendance. The lectures can be held earlier due to the registered requests.
To all they would like to submit seminars or scientific lectures during the third semester of the **I.S.A.R.E.S.T.** (October, November and December) in 2008, you are kindly requested to contact the secretary of the **I.S.A.R.E.S.T.** for date and presentation arrangements of the seminars or lectures. Please, do not hesitate to participate in our activities, this chance might be required by young scientists in our country, IRAQ, to develop and grow as well as introduce the professors and experts in field. You could find us on the post address, emails and mobile below:

Mailing Address:

P. O. Box 55259, Baghdad 12001, IRAQ

Online:

www.ijap.org

editor@ijap.org

editor_ijap@yahoo.co.uk

irq_appl_phys@yahoo.com

Mobile:

00964-7901274190

Saad F. Al-Saffar
Khalil I. Khalaf
Ali N. Abo Raghif

Department of Mechanical Engineering, College of Engineering, Alqadisiyah University, Diwaniyah, IRAQ

Determination of Thermal Conductivity of Compact Graphite Iron

It is presented an experimental study about thermal conductivity in gray iron and compacted graphite iron. Thermal conductivity of the specimen is measured by a comparative method with stationary axial heat flow according to ASTM E 1225. The investigated specimen is put in a stack in tight thermal contact with two reference materials of same diameter. The upper reference specimen is coupled to a heat source, the lower reference to a heat sink. A guard heater and other experimental setup minimize radial heat losses. Reference material is electrolytic iron with certified thermal conductivity. It was tested 2 gray irons, the first alloyed with CuSnCr and the second with CuSnCrMo. Two grades of compacted graphite iron were also tested, CGI 350 and CGI 450. The tests were conducted up to 400°C.

The results show that thermal conductivity decreases in the following sequence: CuSnCr gray iron, CuSnCrMo gray iron, CGI 350, CGI 450. The thermal conductivity results of the gray iron samples decrease with increasing temperatures, and are almost constant for the CGI samples. The results show the potential of using CGI 350 for applications like engine cylinder heads.

Keywords: Thermal conductivity, Cast irons, Compacted graphite iron, Gray iron
Received: 15 June 2008, Revised: 25 August 2008, Accepted: 5 September 2008

1. Introduction

Thermal conductivity is, in some applications, the main reason for the material selection, in special in the automotive industry, for internal combustion engine components and brake systems. Cast irons have been used for such components (cylinder heads, pistons, brake drums and disks), combining good mechanical and friction properties with thermal conductivity [1-3].

The recent use of compacted graphite iron (CGI) for cylinder heads has demanded the study of properties of this material, in special the thermal conductivity. In comparison with gray iron, CGI shows lower values of thermal conductivity, and this is the main reason of the designer objection regarding CGI for such applications, in spite of its higher mechanical properties [4-6]. However, one point is the comparison between the CGI not with the regular gray iron, but with alloyed gray irons (Cu, Sn, Cr, Mo), nowadays used for diesel cylinder heads. In a general way the alloying elements tend to decrease thermal conductivity, so those alloyed gray irons must present thermal conductivity values lower than the regular gray irons. After that, this paper presents a thermal conductivity comparison study between compacted graphite irons and alloyed gray irons [7].

Thermal conductivity values of metallographic phases of cast irons are presented in Table (1). It can be seen that ferrite has higher thermal conductivity than pearlite and also that cementite can lower the cast iron thermal conductivity. Parallel to the graphite basal plane the thermal conductivity is high and, in this condition, is the phase with highest thermal conductivity. So, a graphite shape that eases the thermal conductivity along the basal plane must result in maximum thermal conductivity [8,9].

Table (1) Thermal conductivity of main metallographic phases in cast irons at room temperature [7]

Metallographic constituent	Thermal conductivity ($W\ m^{-1}\ ºC^{-1}$)		
	0–100ºC	500ºC	1000ºC
Ferrite	71–80	42	29
Pearlite	50	44	40
Cementite	7–8	-	-
Graphite (to basal plane)	-	-	-
Parallel	293-419	84–126	42–63
Perpendicular	84	-	-

This is the case of gray iron, as can be seen in Fig. (1). The amount of graphite also affects thermal conductivity, especially in gray irons, as shown in Fig. (2). In this figure theoretical models were plotted considering nodular graphite as perfect spheres and flake graphite as discs. The model for nodular graphite showed

good agreement with the experimental results, while for flake graphite this agreement is poor.

Typical values of thermal conductivity of different gray and ductile irons grades can be seen in tables (2) and (3) for increasing temperatures. For gray irons thermal conductivity decreases with temperature. This trend is observed in many reports [7,10], although there is no discussion on the cause of this behavior. The effect of the temperature in reducing thermal conductivity is higher for gray irons with high carbon content [10].

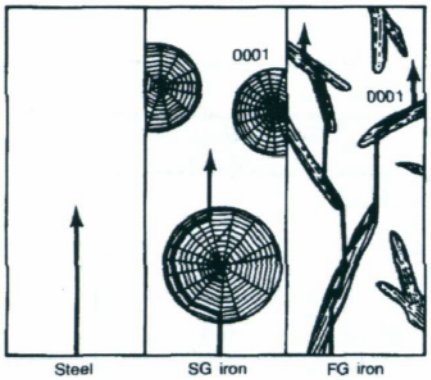

Fig. (1) The thermal conductivity of graphite parallel to basal plane is higher than perpendicular

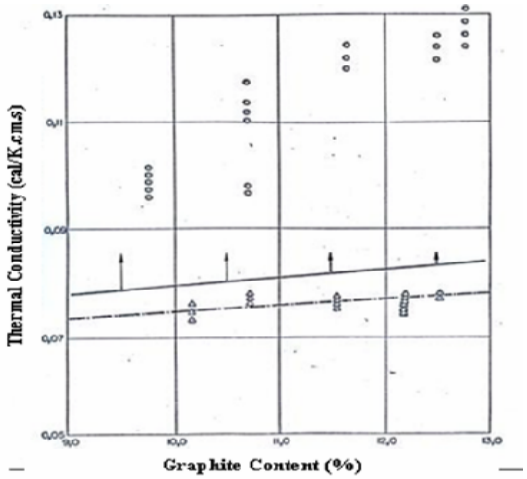

Fig. (2) Effect of graphite amount on the thermal conductivity, for gray iron (O) and ductile iron (□), with ferritic matrix

Table (2) Results of thermal conductivity for different grades of gray Iron

Temperature (°C)	Thermal conductivity (W/K.m)		
	GJL 150	GJL 200	GJL 250
100	52,5	50,8	48,8
200	51,5	49,8	47,8
300	50,5	48,8	46,8
400	49,5	47,8	45,8
500	48,5	46,8	44,8
Temperature (°C)	Thermal conductivity (W/K.m)		
	GJL 300	GJL 350	GJL 400
100	47,4	45,7	44,0
200	46,4	44,7	43,0
300	45,4	43,7	42,0
400	44,4	42,7	41,0
500	43,4	41,7	40,0

As for steels, the presence of alloying elements in cast irons decreases thermal conductivity for a given matrix (it should always be considered that alloying elements can affect the amounts of ferrite and pearlite in the matrix). In table (4) the effects of alloying elements are presented. In this table it can be seen the significant effect of silicon, which is always present in high amounts in cast irons.

Table (3) Results of thermal conductivity for ductile irons

	GGG-35.3	GGG-40	GGG-50
100 ºC	40.2	38.5	36.0
200 ºC	43.3	41.5	38.8
300 ºC	41.5	39.8	37.4
400 ºC	38.8	37.4	35.3
500 ºC	36.0	35.0	33.5
	GGG-60	GGG-70	4 Si-Mo
100 ºC	32.9	29.8	25.1
200 ºC	35.4	32.0	27.2
300 ºC	34.2	31.0	28.1
400 ºC	32.8	30.3	28.6
500 ºC	31.6	29.8	28.9

Table (4) Change in Thermal Conductivity of Gray Iron Upon Addition of 1% Alloying Element [7]

Element	Experimental range %	Change in k, %
Silicon	1 – 6 0.65 – 4.15 (ductile iron)	-6 -14.7
Manganese	0 – 1.5	-2.2
Phosphorus	?	-6
Chromium	0 – 0.39 0 – 0.5	+21 -30
Copper	0 – 1.58	-4.7
Nickel	0 – 0.74	-14.5
Molybdenum	0 – 0.58	-12
Tungsten	0 – 0.475	-5.2
Vanadium	0 – 0.12	0

The thermal conductivity of CGI is compared to an unalloyed gray irons in Fig. (3). It is shown that, in CGI high nodularity decreases thermal conductivity, while increasing temperatures have little effect in this property. Additional results are presented in Fig. (4), where it can be seen that higher nodularity decreases thermal conductivity [11].

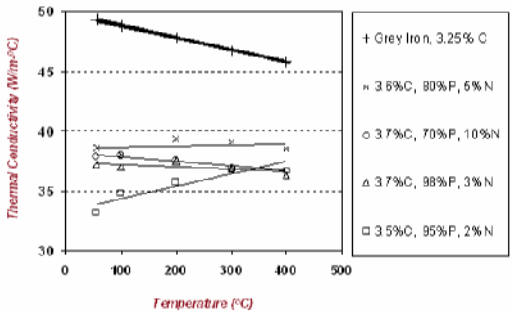

Fig. (3) Thermal conductivity results of compacted graphite iron, compared to a gray iron [12]

A practical consequence of the differences between gray and compacted graphite iron's thermal conductivity was verified, establishing the temperature during the restrain of break discs (Fig. 5). It is observed that gray iron break discs are better heat conductors than CGI, causing the CGI casting to reach higher temperatures in service.

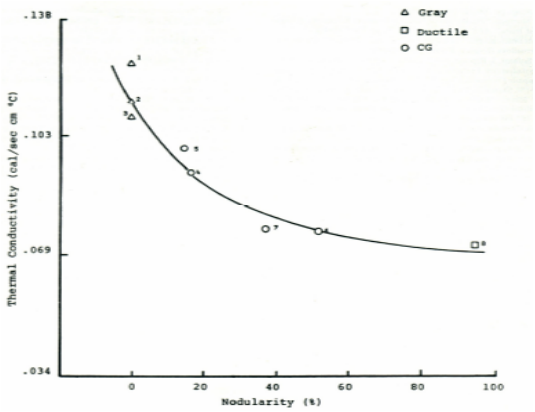

Fig. (4) Effect of nodularity on the thermal conductivity of cast irons [11]

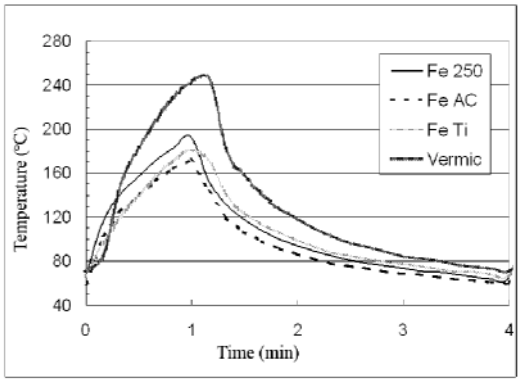

Fig. (5) Temperature of the break disk during the breaking cycles [13]

In the following experimental work thermal conductivities of two alloyed gray irons used for cylinder heads for heavy diesel engines and two classes of CGI were determined.

2. Experimental Procedures

Table (5) shows the chemical composition of the tested materials. Copper and tin are used in CGI to obtain the necessary amount of pearlite for each grade. In gray iron, copper, tin, chromium and molybdenum are used as alloying elements to obtain the high strength grades. Gray iron samples were obtained from bars with 30 mm diameter, and CGI samples were machined from keel blocks of 25 mm, casted in chemically bonded sand moulds. Those are standards samples for tensile tests.

Thermal conductivity was measured by a comparative method with stationary axial heat flow according to ASTM E 1225-99 [14]. The investigated specimen is put in a stack in tight thermal contact with two reference materials of the same diameter. The upper reference specimen is coupled to a heat source, the lower reference to a heat sink. Radial heat losses are minimized by a guard heater and other experimental setup. Reference material is electrolytic iron with certified thermal conductivity.

Table (5) Chemical composition of CGI and Gray Iron samples

Elements	CGI 350	CGI 450	Gray Iron 250	Gray Iron 300
C (%)	3.65	3.62	3.43	3.30
Si (%)	2.45	2.41	2.07	2.05
Mn (%)	0.37	0.37	0.55	0.56
Cu (%)	0.41	1.17	1.00	1.20
Sn (%)	0.031	0.064	0.10	0.11
Cr (%)	0.029	0.029	0.20	0.24
Mo (%)	-	-	-	0.30

Table (6) Microstructure and mechanical properties of the CGI samples

	CGI 350	CGI 450	Gray Iron 250	Gray Iron 300
Ferrite (%)	48	2	0	0
Graphite shape	4% nodulary	7% nodularity	A, size 4	A, size 4
UTS (MPa)	371	498	270	317
YS (MPa)	292	443	-	-
E (%)	2,5	1,4	-	-

The temperature drop along the specimen ΔT_p and the references ΔT_{R1}, ΔT_{R2} as well as the distances between the temperature sensors Δx_p, Δx_{R1} and Δx_{R2} are measured. With known thermal conductivity dlu,] as function of temperature of the reference material λ_{R1} and λ_{R2}, following equation gives the thermal conductivity of the specimen λ_P

$$\lambda_P = \frac{1}{2}\frac{\Delta x_P}{\Delta T_P}\left[\left(\lambda_{R1}\frac{\Delta T_{R1}}{\Delta x_{R1}}\right)+\left(\lambda_{R2}\frac{\Delta T_{R2}}{\Delta x_{R2}}\right)\right] \qquad (1)$$

An apparatus of Dynatech Co., Cambridge, MA, USA, Type TCFCM was used for the measurements. Temperature was measured by Ni-CrNi thermocouples, thermo-voltages were measured by a data acquisition system Philips, Type PM 8237A, which automatically references to ice point and linearizes the signal. A traveling microscope measured the distances of the drillings of the specimen, where the thermocouples are placed.

The temperature difference in the specimen is approximately 10°C. The average value of the two temperature values measured along the specimen is considered as specimen temperature.

3. Results and Discussion

Table (7) and Fig. (6) show the results obtained. The numbers are the average of 2 measurements. The results show that gray iron presents always higher thermal conductivity than

CGI. The differences decrease with increasing temperature, because for gray iron thermal conductivity results decrease with increasing temperature, while for CGI the results do not show a significant variation with the temperature. The highly alloyed Gray Iron Grade 300, used for cylinder heads of heavy diesel engines, presents lower thermal conductivity than the Gray Iron Grade 250. This is caused by the lower carbon content and by the alloying elements, reducing thermal conductivity.

Table (7) Thermal conductivity results

Temperature (°C)	Thermal conductivity (W/K.m)			
	CGI 350	CGI 450	Gray Iron 250	Gray Iron 300
100	37,0	33,6	50,0	45,5
200	37,4	34,2	46,6	43,15
300	37,2	34,3	43,6	41,2
400	36,5	33,9	40,9	39,7

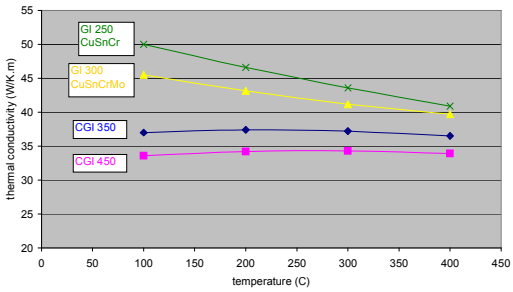

Fig. (6) Thermal conductivity results of CGI and Gray Iron

Comparing with the results on Table (2), the effect of temperature, reducing the thermal conductivity of gray irons, is much higher in the results we obtained (Fig. 6). One possible reason for that is that the carbon content from our samples (3,3-3,5) is higher than the usual carbon contents of gray iron (3,2-3,4), resulting in higher amount of graphite (lamellar).

Comparing the two grades of CGI (Fig. 6), one can observe that the CGI Grade 350 should be consider a candidate material for cylinder heads, because of the higher thermal conductivity compared to the CGI Grade 450. In this case, the larger amount of ferrite in the CGI Grade 350 resulted in increasing thermal conductivity.

4. Conclusions

From the obtained results, we can conclude the following. Gray iron always presents higher thermal conductivity comparing with compacted graphite iron, due to the graphite form. Increasing the temperature and adding alloying elements, thermal conductivity decreases for gray irons. CGI 350 presents higher thermal conductivity comparing with CGI 450, due to the higher ferrite content.

References

[1] R.B. Gundlach, *AFS Trans.*, (1983) 389.
[2] S.Y. Buni, "Investigation of wear and thermal cycling characteristics of cast irons with dissimilar forms of graphite", Ph.D. thesis, Indian Institute of Bangalore, Bangalore (1994).
[3] B.M. Drapkin, A.A. Zhukov and Y.V. Piguzov, *Met. Sci. Heat Treat.*, 15 (1973) 964–966.
[4] R.B. Gundlach, *AFS Trans.*, 86 (1978) 55–64.
[5] R.B. Gundlach, *AFS Trans.*, 87 (1979) 551–560.
[6] T.L. Oberle, *J. Metals*, 3 (1951) 438–439.
[7] D. Stefanescu, "Physical properties of cast iron", in: Goodrich, G.M., **"Iron Castings Engineering Handbook"**, AFS (2003).
[8] K. Roehrig, *AFS Trans.*, 86 (1978) 75–88.
[9] M.M. Shea, *AFS Trans.*, 86 (1978) 23–30.
[10] H.T. Angus, *BCIRA J.*, (1960) 126-134.
[11] R.W. Monroe and C.E. Bates, *AFS Trans.*, (1982) 615.
[12] S. Shao et al., *Sintercast* (1997).
[13] Y.J. Park et al., *AFS Trans.*, 93 (1985) 415–422.
[14] Thermal conductivity of solids by means of the guarded-comparative-longitudinal heat flow technique, ASTM E 1225 -99.

This article was reviewed at Faculty of Materials Engineering, National University of Singapore, SINGAPORE and School of Applied Sciences, University of Technology, Baghdad, IRAQ

Ali M. Mousa
Shams B. Ali

Materials Research Unit,
School of Applied Sciences,
University of Technology,
Baghdad, IRAQ

Effects of Deposition Parameters on Chemically Deposited PbS Thin Films

Lead sulfide thin films were deposited by chemical bath deposition onto glass substrates. Depending on the percentage of the constituent bath salts and bath temperature, films with polycrystalline or amorphous structure were obtained. The influence of bath temperature and bath percentage on optical transmittance in the NIR region and structure was investigated. It was found that thickness goes on decreasing as the concentration of lead acetate increases. XRD revealed that the film deposited at 20°C displays no obvious characteristic reflection peaks which could be detected. Large grains are obtained when both deposition time and temperature are increased.

Keywords: Porous silicon, Electrical conductivity, Transport mechanisms, Modeling
Received: 18 June 2008, Revised: 17 August 2008, Accepted: 24 August 2008

1. Introduction

Lead sulfide (PbS) Bulk and thin films are one of the earliest semiconductors extensively studied in the last decades, due to their potential for IR detector materials [1,2], quantum dots applications [3], selective coating for photothermal conversion [4], solar cell [5]. PbS is a direct narrow energy gap semiconductor and its energy gap at room temperature is about (0.37-0.4) eV. Also, lead sulfide having a positive temperature coefficient of the energy gap among all other semiconductor which shows a negative temperature coefficient [6]. PbS thin films can be obtained by several methods [7-9]. Chemical bath deposition is mostly used [7,10-13], since it is a very comfortable method for deposition of polycrystalline films, at low cost with a good quality of the obtained films [14]. Also, by changing the percentage of lead sulfide, which is co-deposited with cadmium sulfide, a new semiconductor material is prepared [15-17].

In this work, we try to re-evaluate and discuss the effect of different deposition parameters on the physical properties of deposited PbS thin films.

2. Experiment

The samples studied were thin polycrystalline films of PbS layers prepared by CBD on commercial glass slides with dimensions ($1x26x76mm^3$).The substrates were washed with distilled water in ultrasonic bath and then immersed for 24 hours in chromic acid (1gm of CrO_3 in 20ml of distilled water) and finally washed again with distilled water. The aqueous solution of the deposition bath was prepared by the sequential addition of 5ml of 0.5M lead acetate, 5ml of 2.0M KOH, 6ml of 1.0M thiourea and 2ml of 1.0M triethanolamine in 100ml beaker. The total volume was completed to 100ml with distilled water. First, potassium hydroxide was added to the lead acetate and mixed by magnetic stirrer, the color change rapidly to white and this indicate the formation of lead hydroxide (Eq. 1). Thiourea was added to the solution and then T.E.A was gradually added with continuous stirring as the color changes to brown and finally into gray black. A metallic layer will deposit on the beaker walls. The slides were immersed in the solution vertically where the PbS is deposited (Eq. 2).

$Pb(CH_3COO)_2+KOH \rightarrow Pb(OH)_2+K(CH_3COO)$ (1)

$Pb(OH)_2+SC(NH_2)_2 \rightarrow PbS$ + another compound (2)

Thickness measurements were made by optical method using He-Ne laser with incident angle 45°. The film thickness (t) is calculated using

$$t = \frac{\lambda}{2}\frac{\Delta X}{X} \quad (3)$$

where ΔX the width of dark fringes and X is the width of light fringes

Optical transmission and absorption measurements were performed at room temperature at (1000-4000)nm range using IR spectrophotometer. Values of energy bandgap (E_g) were calculated from the extrapolated intercept of $(\alpha h\upsilon)^2$ versus $h\upsilon$, and absorption coefficient was calculated from transmission spectra using Beer-Lamberts law

$$\alpha = \frac{1}{t}\ln\frac{1}{T} \quad (4)$$

where t is the film thickness and T is the transmission

For the electrical measurements, aluminum electrodes in a coplanar configuration were

 ISSN 1813-2065

evaporated in vacuum on the surface of the PbS films. The distance between electrodes was 7mm. The activation energies of samples deposited at different conditions were deduced from ln$I$ vs. $1/T$ curves. The structural properties of the layers were investigated by X-ray measurements using Philips-PW 1840 XRD system, which has the following characteristics: the CuKα with 1.54Å wavelength, 3 deg/min scanning speed, 10°-60° incidence angle. Average grain size ($G.Z$) was deduced using Scherer equation

$$G.Z = \frac{0.9\lambda}{B\cos\theta} \qquad (5)$$

where λ is the wavelength of radiation, B is the full width half maximum (FWHM), θ is Bragg diffraction angle

Table (1) The deposition conditions

Bath composition	$Pb(CH_3COO)$	$SC(NH_2)_2$	KOH	T.E.A	
T °K	293	308	313	323	
pH	9.6	10.4	11.7	12.3	
t(hr)	2	2.5	3	3.5	4
M $Pb(CH_3COO)$	1	0.9	0.7	0.5	
M $SC(NH_2)_2$	0.2	0.4	0.6	0.8	
M KOH	1	1	1	1	
M T.E.A	1	1	1	1	

3. Results and Discussion

Fig. (1) shows the dependence of the film thickness on deposition parameters. The film thickness goes on decreasing as the concentration of lead acetate increases as shown in Fig. (1a). This parameter attained a state of higher super saturation earlier, generating precipitate instead of film. By keeping 0.5 mol.L^{-1} concentration of lead acetate, the concentration of thiourea was optimized. Fig. (1b) shows the thickness of PbS film variation with concentration of thiourea. It is found that the maximum value of thickness is at 1mol.L^{-1} concentration, which is taken as optimized value. By taking the above optimized value of concentrations, the terminal thickness of PbS with deposition time is shown in Fig. (1c).

Two different stages could be distinguished; the initial with rate linear up to 3 hrs reaching a value of 617nm, after which a quasi saturation stage starts, where the growth rate is reduced in the deposition range (3-4) hours. Such trend could be attributed to the constituent ions (Pb^{+2} and S^{-2}) which start to deplete from the bath [18], hence the growth of the film proceeds slowly and thickness slowly increases with prolonged immersion of substrates in the deposition bath. The growth kinetics was also studied by keeping the deposition time and pH value constant and changing the bath temperature. The variation in thickness function of bath temperature is shown in Fig. (1d).

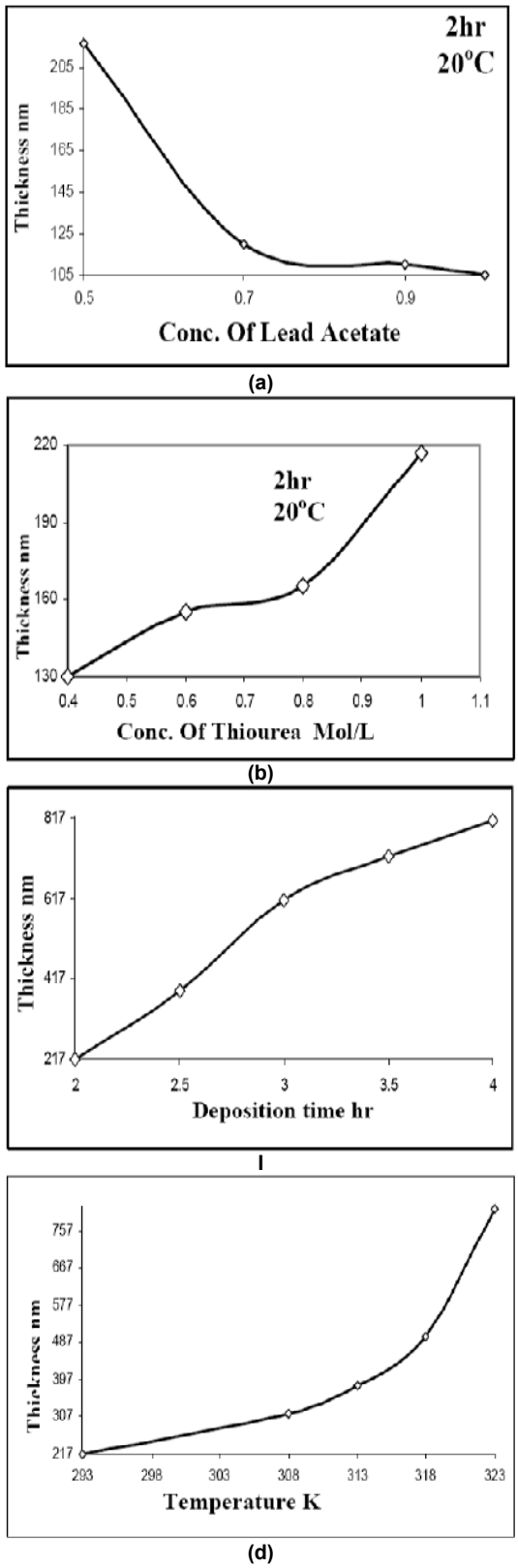

Fig. (1) Characteristics of film thickness (a) as a function of lead acetates, (b) as a function of thiourea, (c) terminal thickness as a function of deposition time, and (d) as a function of temperature

Thickness of the films was found to increase exponentially with temperature. Increasing bath temperature considerably shortens the deposition period. The growth of 757nm film at 500°C requires 2 hrs while requires more than 4h at 200°C. The increasing of bath temperature leads much probably to greater mobility of both constituent atoms on the substrate, leading to greater mobility of their recombination to form PbS.

From the XRD results, the orientation of the planes is determined as well as the average grain size of PbS films is estimated. The XRD patterns of the as-deposited films for different deposition conditions are shown in Fig. (2). For films deposited at 200°C, Fig. (2a) displays no characteristic reflection peaks which could be detected in the XRD patterns.

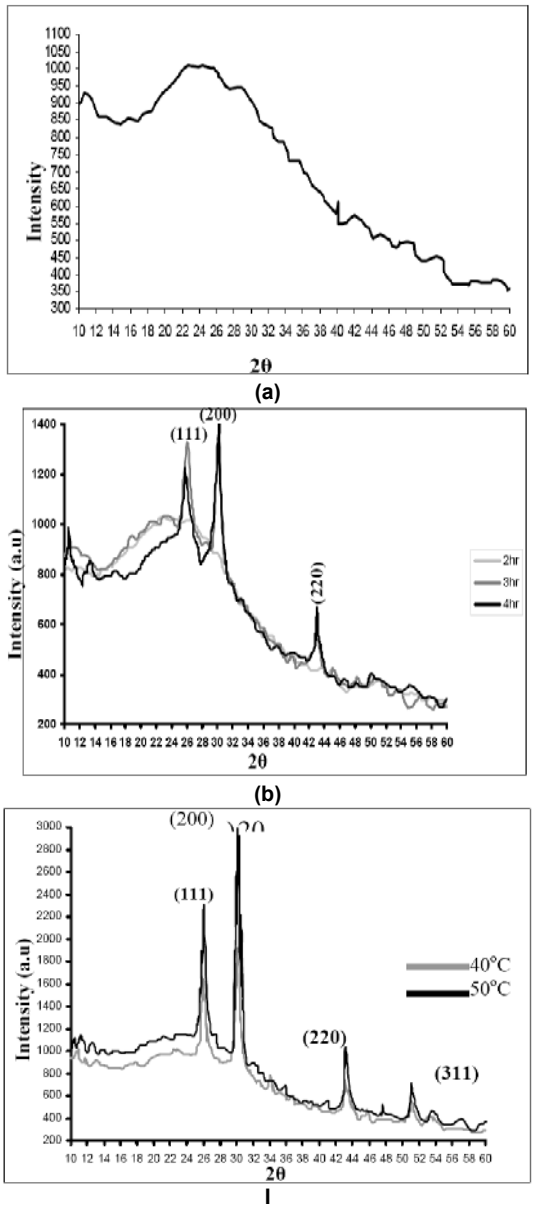

Fig. (2) The XRD results of deposited films (a) at 20°C and 2 hrs, (b) at different times and (c) at different temperatures

When deposition time and bath temperature are increased, the prepared films will be polycrystalline. The XRD patterns in Fig. (2b,c) display four different peaks at 2θ values of approximately 26°, 30°, 43° and 57° corresponding to the (111), (200), (220) and (311) crystalline planes of cubic phase respectively, which indicates that PbS films are well crystallized. The intensity of (200) peak is higher than that of (220) peak indicating that there is a (200) preferred orientation during the deposition. Such kind of preferred orientation has been recently reported for nanowires [19].

The dominated orientation can be explained using the survival of the fastest model [20]. According to this model, nucleation with various orientations can be formed at the initial stage of deposition. Each nucleus competes to grow but only nuclei having the fastest growth rate can survive. The principal driving force for grain growth is the reduction of the grain boundary surface area per unit volume [21]. Fig. (3) shows the dependence of average grain size on the deposition time and bath temperature. When both parameters increase, large grains are obtained in linear dependences, with quasi saturation at higher values. It seems that these two parameters are a necessary condition to obtain a polycrystalline films.

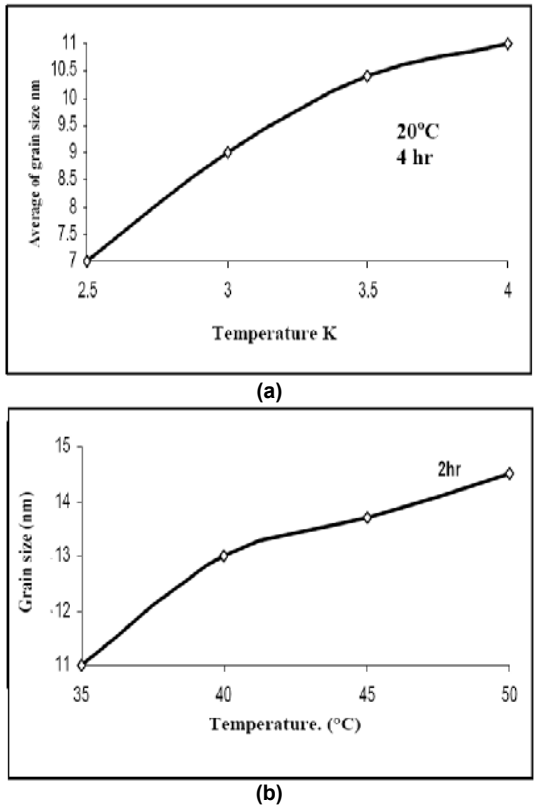

Fig. (3) Grain size as a function of temperature at deposition time of (a) 4 hrs and (b) 2 hrs

However, the deposition time produces larger increase in the grain size. It is obvious that

ISSN 1813-2065

increasing thickness with time is due to the increasing grain size, while increasing bath temperature increases the number of deposited layers.

The measurement of the transmission of all thin film samples were carried out in the wavelength range (1000-4000) nm at room temperature. Fig. (4) displays the transmission spectra at different deposition conditions. At the absorption edge, the curves are exponential, which is probably an indication of the homogeneity of the films and the presence of normal band structure [21].

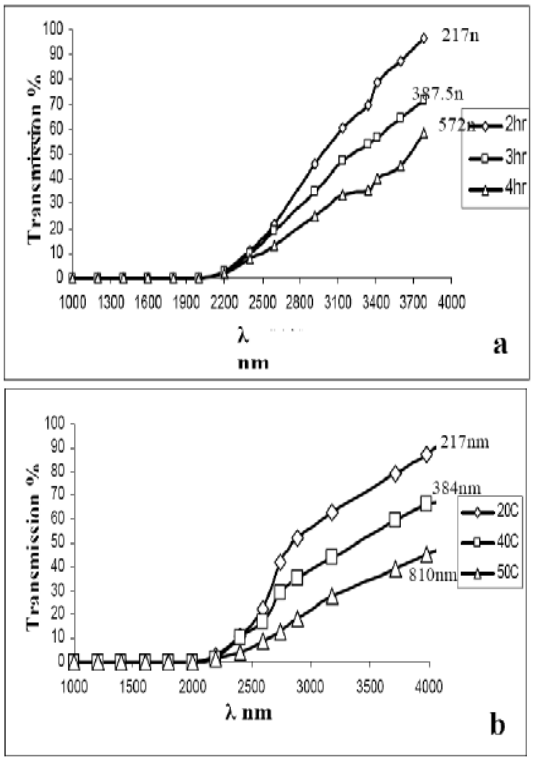

Fig. (4) Spectral transmission as a function of (a) deposition time and (b) bath temperature

From the plots of $(\alpha h\upsilon)^2$ versus $h\upsilon$ in Fig. (5), the dependence is almost linear in the higher energy region. This indicates the direct bandgap transition; therefore, the extrapolation of the straight line portion of the curves to zero absorption gives the corresponding value of bandgap.

Dark electrical conductivity (δ) of the lead sulfide film was measured by using a dc two-point probe method. The variation in versus $1000/T$ for the film is shown in Fig. (6). The electrical conductivity increases with increasing temperature. The dark electrical conductivity at room temperature was of the order of $6x10^{-5}$ $(\Omega.cm)^{-1}$ close to the earlier reported values.

4. Conclusion

In this investigation, PbS thin films were grown on glass substrates by CBD and the effects of growth conditions such as the molarity of the constituents, growth temperature and growth time, on structural and optical properties were studied. The major findings are

1- Film thickness ranged from 217nm to 750nm, and the grain size from 7nm to 15nm, depending on the growth conditions

2- NIR optical experiments showed that the energy gap was (0.32-0.38)eV

3- The films deposited at room temperature and 2 hrs deposition time are amorphous

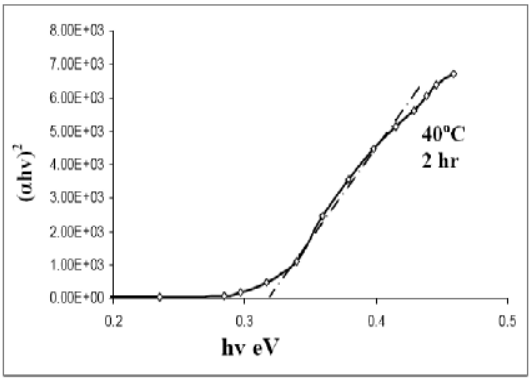

(a)

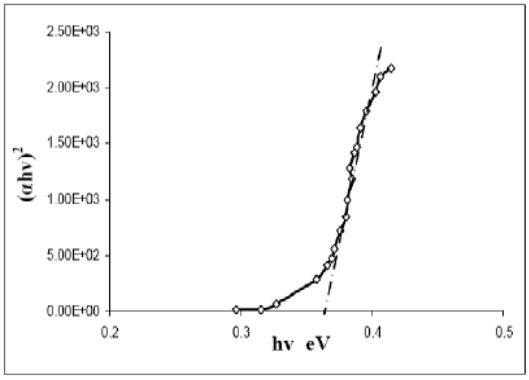

(b)

Fig. (5) Variation of $(\alpha h\nu)^2$ versus $h\nu$ (a) at 40°C and 2 hrs and (b)

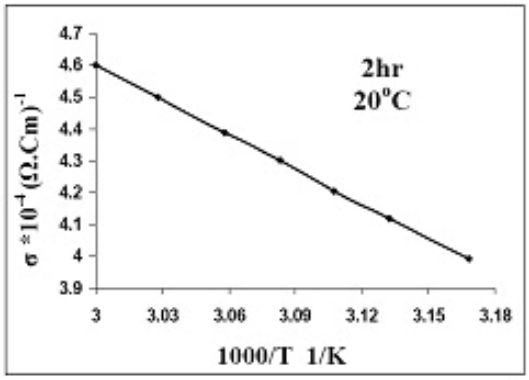

Fig. (6) The electrical conductivity versus temperature

References

[1] M.S. Ghamsari, M.K. Araghi and S.J. Farahani, *Mater. Sci. Eng. B*, 133 (2006) 113.

[2] H. Zhang, D. Yang and J. Niu, *J. Cryst. Growth*, 246 (2002) 108.
[3] A.M. Malyarevich et al., *J. Non-Cryst. Solids*, 353 (2007) 1195.
[4] T.K. Chaudhuri, *Int. J. Ener. Res.*, 16 (1992) 481.
[5] S. Gunes et al., *Solar Energy Mater. Solar Cells*, 91 (2007) 420.
[6] R.K. Das, S. Sahoo and G.S. Tripathi, *Semicond. Sci. Technol.*, 19 (2004) 433.
[7] I. Pop et al., *Thin Solid Films,* 307 (1997) 240.
[8] A.A. Preobrajenski and T. Chasse, *Appl. Surf. Sci.*, 142 (1999) 394.
[9] C. Li et al., *Mater. Lett.*, 61 (2007) 1809.
[10] O. Teran and R.A Sotelo-Lerma, *Thin Solid Films*, 343-344 (1999) 587.
[11] E. Pentia et al., *J. Optoelectron. Adv. Mater.*, 3 (2001) 525.
[12] J.J. Valenzuela-Jauregui et al., *Thin Solid Films*, 441(2003) 104.
[13] H. Zhang and D. Yang, *J. Cryst. Growth*, 263 (2004) 372.
[14] R.K. Das, S. Sshoo and G.S. Tripathi, *Semicond. Sic. Tachnol.*, 19 (2004) 433.
[15] M. Gugliemi et al., *J. Sol-Gel Sci. Technol.*, 11 (1997) 229.
[16] E. Pentia et al., *J. Electrochem. Soc.*, 151 (2004) G729.
[17] H. Li et al., *Proc. SPIE*, 3899 (1999) 376.
[18] P.P. Hankare et al., *Semicond. Sci. Technol.*, 19 (2004) 277.
[19] C. Wu et al., *Mater. Lett.,* 61(25) (2007) 4659.
[20] A. Drift, *Phillips Res. Rep.*, 22 (1967) 267.
[21] K. Kurzydlowski and B. Ralph, **"The Quantitative Description of the Microstructure of Materials"**, CRC Press (1995).

This article was reviewed at Clean Energy Research Center, Korean Institute of Science and Technology, Seoul, Korea, Department of Physics, D.Y. Patil University, Kolhapur, INDIA, and School of Applied Sciences, University of Technology, Baghdad, IRAQ

Nobel Prize in Physics 2008

Nobel Prize in Physics 2008 was won by **Prof. Yoichiro Nambu** and **Prof. Makoto Kobayashi**. Below is a summary of works of both laureates.

Prof. Y. Nambu from the Enrico Fermi Institute, University of Chicago shares the prize for the discovery of the mechanism of spontaneous broken symmetry in subatomic physics.

"The really bold assumption that Nambu now made in 1960 [44] was that spontaneous symmetry breaking could also exist in a quantum field theory for elementary particles." – Scientific Background on the Nobel Prize in Physics 2008

[44] Y. Nambu, "A 'Superconductor' Model of Elementary Particles and its Consequences", in Broken Symmetries, Selected Papers by Y. Nambu, (World Scientific,1995), p.110.

QUARKS: Frontiers in Elementary Particle Physics

by **Y Nambu** *(Univ. Chicago)*

The book explains in a precise and complete manner how elementary particle physics has evolved over the past 50 years. The historical development of the ideas that have shaped our thinking about the ultimate constituents of matter is traced out.

BROKEN SYMMETRY: Selected Papers of Y Nambu

edited by **T Eguchi** *(University of Tokyo, Japan)* & **K Nishijima** *(Chuo University, Japan)*

This book contains selected papers of Prof Nambu who is one of the most original and outstanding particle theorists of our time. This volume consists of about 40 papers which made fundamental contributions to our understanding of particle physics during the last few decades.

Nonlocal Separable Solutions Of The Inverse Scattering Problem

Tony Gherghetta; Yoichiro Nambu

International Journal of Modern Physics A (IJMPA) Volume: 8 No: 18 Year: 1993 pp. 3163-3184

Prof. Makoto Kobayashi from the High Energy Accelerator Research Organization, Japan shares the prize with Prof. Toshihide Maskawa from Kyoto University. The duo are honored for their discovery of the origin of the broken symmetry which predicts the existence of at least three families of quarks in nature.

A GARDEN OF QUANTA: Essays in Honor of Hiroshi Ezawa

edited by **J Arafune** *(National Institute for Academic Degrees, Japan)*, **A Arai** *(Hokkaido University, Japan)*, **M Kobayashi** *(Accelerator Research Organization(KEK), Japan)*, **K Nakamura** *(Meiji University, Japan)*, **T Nakamura** *(Sundai Preparatory School, Japan)*, **I Ojima** *(Kyoto University, Japan)*, **N Sakai** *(Tokyo Institute of Technology, Japan)*, **A Tonomura** *(Hitachi Ltd, Japan)* & **K Watanabe** *(Meisei University, Japan)*

This book is a collection of reviews and essays about the recent wide-ranging developments in the areas of quantum physics. The articles have mostly been written at the graduate level, but some are accessible to advanced undergraduates. They will serve as good introductions for beginning graduate students in quantum physics who are looking for directions. Aspects of mathematical physics, quantum field theories and statistical physics are emphasized.

Carmen Gonzalez

Alcatel R&I – Laboratoire OPTO+, Route de Nozay, F-91460 Marcoussis Cedex, FRANCE

Performance Comparison of InP-Based Phototransistors to PIN and UTC Photodiodes

The main characteristics of vertically illuminated InP/InGaAs-based heterojunction bipolar phototransistors (photo-HBT) developed at OPTO+ (Alcatel) were presented. Also, the design and fabrication of photo-HBT-based monolithically integrated circuits such as optoelectronic amplifier and mixers are described. Comparisons of some performances between photo-HBTs, PIN and UTC photodiodes are commented.

Keywords: InP-based devices, Phototransistors, PIN photodiodes, UTC devices
Received: 18 June 2008, Revised: 22 August 2008, Accepted: 29 August 2008

1. Introduction

InP/InGaAs photo-HBT has been studied for several years [1-3] because of its potential as a high-performance photodetector at micro- or millimeter-wave frequency. Also, photo-HBTs can operate as optoelectronic mixers or photo-oscillators [4] and applications in optical access networks and others microwave photonic systems as radar, passive imaging and remote sensors are becoming possible. Because top illuminated photo-HBT has the same layer structure as single HBT (SHBT), monolithically integrated photoreceivers can be fabricated using the same epitaxial and processing steps, avoiding a regrowth process with its problems. In this paper, we describe the recent developments on top illuminated photo-HBT and its integration in a narrow band amplifier and upconverting mixers, operating in the microwave and millimeter wave bands. Several different approaches for photodetection are proposed. Conventional approach uses PIN photodiodes and, recently, UTC photodiodes are proposed for their excellent high-power performances. In the last part of this paper, PIN and UTC photodiodes performances, reported in the literature, are comparatively commented with those of photo-HBTs.

2. InP/InGaAs photo-HBT

The n-p-n InP/InGaAs photo-HBT is a three-terminal device with a structure similar to the HBT. Also, its operation mode is nearly identical to and related to that of the HBT. So, higher frequency performance for the photo-HBT should be feasible as was demonstrated in recent reports. InP-based photo-HBT consists of an n-type wide band-gap InP emitter, a heavily doped p-type InGaAs base, and a lightly doped n-type InGaAs collector. In top illuminated photo-HBTs, the optical window is placed directly in the base region, and the photo-HBT operates as an HBT amplifier in the common emitter-mode operation, with a photodiode formed by the base-collector junction. The schematic diagram shown in Fig. (1) illustrates the layer structure of the device.

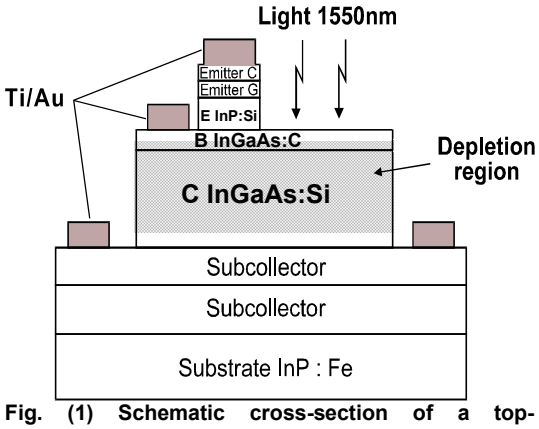

Fig. (1) Schematic cross-section of a top-illuminated photo-HBT

Photo-HBT performances were improved in terms of the optical gain cut-off frequency (F_c) and optical gain (G_{opt}) via three types of optimization [5]: (1) A compositionally graded-base to improve the (photo) current gain. (2) The reduction of the device size down to the limit of our technology to improve the dynamic characteristics. That was obtained for photo-HBT with a base-collector junction area of 46μm^2, an emitter area of 9μm^2 and an optical window area of 16 μm^2, presented in the next section. (3) Base contact behind the emitter mesa, opposite to the optical window, to minimize the "leak" photocurrent.

ISSN 1813-2065

3. InP/InGaAs photo-HBT performances

As a direct photodetector

Fig. (2) displays the frequency photoresponse of the optimized photo-HBT, measured at a wavelength of 1.55µm. The light intensity was externally modulated by a RF signal ranging from 130MHz to 20GHz. The device exhibits a G_{opt} of 32dB at 130MHz, and a F_c of 110GHz. The DC responsivity (R_{DC}) was 0.2A/W.

We measured the RF output power dependence on the input light power at 19GHz, as shown in Fig. (3). The dependence is linear up to 2dBm input light power and the highest RF output power obtained before saturation was –21dBm.

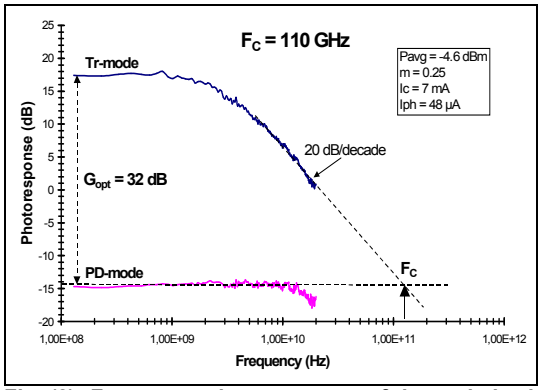

Fig. (2) Frequency photoresponse of the optimized photo-HBT

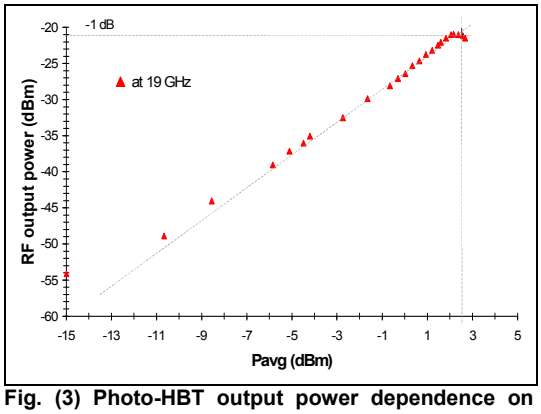

Fig. (3) Photo-HBT output power dependence on input light power, at 19 GHz

The analog noise performance of the photo-HBT was characterized by measuring the output noise power spectral density as a function of frequency and using the measured frequency response to compute the total equivalent noise current spectral density $\langle I_{in} \rangle$ referred at the optical input of the photo-HBT. Fig. (4) shows the input-referred noise current spectral density measured from 1 to 40GHz, at the collector current (I_c) of 2 and 10mA.

In Fig. (4), the solid lines are the tendency curves of experimental measurements. At 28GHz, $\langle I_{in} \rangle$ of the photo-HBT was 51 and 36 pA/Hz$^{1/2}$ for the 10 and 2mA collector current, respectively. At 40 GHz, $\langle I_{in} \rangle$ increases to 66 and 50 pA/Hz$^{1/2}$ for I_c equal to 10 and 2mA, respectively. To assess the digital performance of photo-HBTs a system evaluation was performed using a packaged phototransistor of first generation with an R=0.35A/W and a f_c=65GHz.

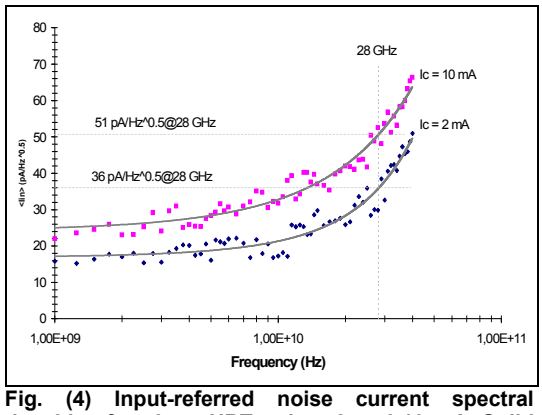

Fig. (4) Input-referred noise current spectral densities for photo-HBT at Ic = 2 and 10 mA. Solid lines are the tendency curves of experimental measurements

The device was evaluated using a self-heterodyne optical mm-wave source. It supplies, both an intermediate frequency at 2GHz modulated in a 16 QAM modulation scheme at a symbol rate of 6.25Msps (25Mb/s), and a reference signal at 29.875GHz. The performance of the photo-HBT was evaluated in terms of bit error rate (BER) versus the carrier to noise ratio (C/N). The results are presented in Fig. (5) one curve shows the reference performance at 800MHz, while the second one shows the performance at the 27.875GHz carrier: a BER of 10^{-9} for a C/N of 24.3dB was achieved.

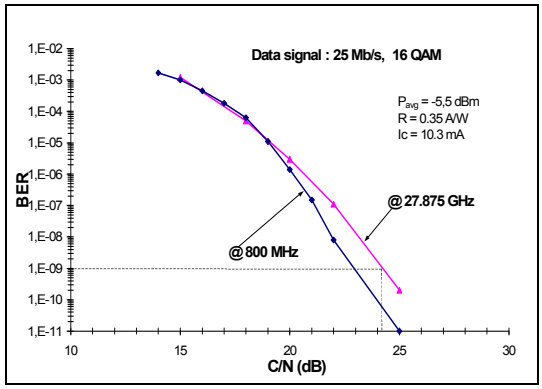

Fig. (5) BER performance of the photo-HBT as a direct photodetector

3.2 As an upconverting mixer

We have taken advantage of the inherent non-linear properties of the photo-HBT to achieve upconversion of an intensity modulated optical signal at the intermediate frequency (IF) of 2GHz to the 28 and 42GHz frequencies, using a local oscillator (LO) signal at 26 and 40GHz, respectively. The performance of the photo-HBT

mixer was evaluated in terms of the mixer conversion gain (G_{conv}), which was equal to 10 and 6dB at 28 and 42GHz, respectively.

4. Optoelectronic integrated circuits – OEIC

A narrow-band photoreceiver OEIC working in the 28GHz regime was fabricated at OPTO+. The fabricated OEIC is depicted in Fig. (6). It consists of two enabil cells and two matching cells as shown in Fig. (6). The first enabil cell consists of one photo-HBT and one HBT and the second one is composed of two HBTs. The matching cell placed between the enabil cells was designed in order to maximize the power gain of the circuit at 28GHz and the other one provides the 50Ω matching output. The two matching cells include MIM capacitors, coplanar lines and resistors [5].

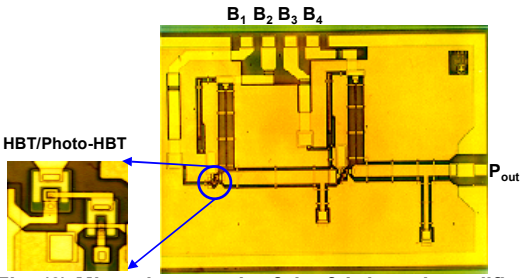

Fig. (6) Microphotograph of the fabricated amplifier circuit. The chip size was 2400x1600 µm2

As depicted in Fig. (7), the 28GHz narrow-band amplifier exhibits a 4GHz bandwidth around the center frequency of 28GHz and a transimpedance gain (G_{TZ}) of 50dBΩ was measured.

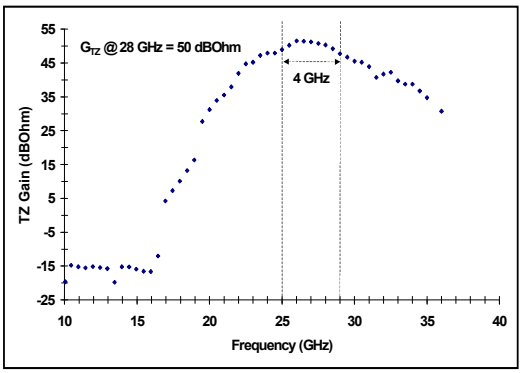

Fig. (7) Frequency response of the 28 GHz amplifier circuit in terms of transimpedance gain

Using a packaged circuit, a system evaluation was made. For this experiment, the light intensity was externally modulated using a subcarrier at 27.875 GHz and encoded with a 16 QAM, 25 Mbit/s data signal. Fig. 8 displays the BER performances of the amplifier circuit as a function of the carrier to noise ratio for a 27.875 GHz subcarrier. A BER of 10^{-9} for a C/N of 24.3 dB was achieved and no error floor emergence was observed. For comparison, the C/N response of a PIN photodiode with a bandwidth of 60 GHz and a DC responsivity of 0.25 A/W is shown.

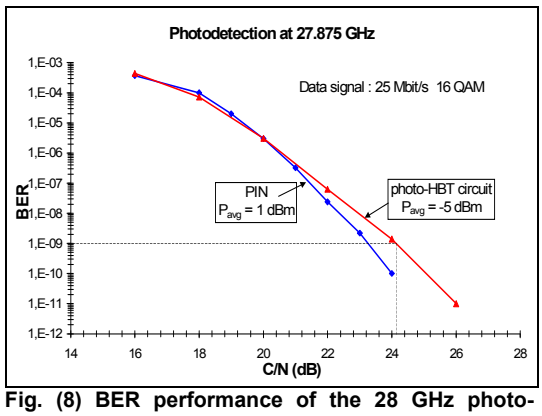

Fig. (8) BER performance of the 28 GHz photo-HBT/HBT photoreceiver

Another photoreceiver using a phototransistor based on a double HBT has been proposed recently by Kamitsuna et al. [6]. They fabricated a photo-DHBT/DHBT broadband photoreceiver with a bandwidth of 40 GHz, consisted of one photo-DHBT followed by a reactively matched 2-stages DHBT amplifier.

For performing frequency change from the intermediate frequency of 2 GHz to the upconverted 28 or 42 GHz frequency, two types of monolithically integrated mixers were designed and fabricated. Type I mixer consists of a photo-HBT surrounded by two matching cells, and type II mixer consists of two enabil cells and three matching cells. The O/E mixers were evaluated in terms of the mixer conversion gain, Gconv, and the results are shown in Table 1. For comparison, Gconv of the individual photo-HBT are also shown in the same table [5].

Table (1) Mixer gain conversions of individual photo-HBT and mixer circuits of types II and I

	G_{conv} at 28 GHz	G_{conv} at 42 GHz
individual photo-HBT	10 dB	6 dB
Type I mixer	12 dB	9 dB
Type II mixer	17 dB	–

5. Performances of PIN and UTC photodiodes

The main attraction of top-illuminated PIN photodiodes has been its compatibility for integration with single heterojunction transistors in photoreceivers OEICs [7,8]. However, the drawback of this approach is a speed limiting tradeoff between diode depletion layer capacitance and transistor transit time. The potential of this simple approach has been demonstrated recently with a monolithically

ISSN 1813-2065

integrated PIN/SHBT photoreceiver with –3dB-bandwidth of 53 GHz, using a PIN photodiode with a DC responsivity of 0.32 A/W, a –3dB-bandwidth of 33 GHz and an absorption layer thickness of 400 nm. When the PIN photodiode absorption layer thickness increases to 600 nm, the –3dB bandwidth of the PIN/SHBT photoreceiver decrease to 30 GHz [7]

For higher-speed operation, waveguide (WG-PD) or traveling-wave (TW-PD) photodiodes with light incident parallel to the junction plane has been proposed. Although reported bandwidths of these photodiodes can achieve frequencies above 100 GHz, photoreceivers based on this type of photodiodes exhibit similar bandwidths to those obtained with PIN/SHBT designs.

For high-speed communication systems, optical amplifiers can be installed directly in front of the photoreceiver. In this approach, fast photodetectors with high saturation power are necessary. In addition, the use of high-output-power photodiodes can eliminate the post amplification circuit. Uni-traveling-carrier (UTC) photodiode, which has a p-type photoabsorption layer, a wide-bandgap depletion layer and only fast electrons act as active carriers, exhibits very fast response and a good linearity at optical powers of 100mW order. However, since UTCs generally require a thin absorption layer, quantum efficiency is relatively low in back illuminated devices. Responsivity of 0.16A/W, bandwidth of 114GHz and an output peak-to-peak voltage (V_{p-p}) of 1.9V, using an absorption layer thickness of 140nm, has been reported [9]. In order to improve the responsivity, edge-illuminated UTC-PDs are necessary. For example, an edge-illuminated refracting-facet UTC-PD with a maximum responsivity of 0.4A/W, a bandwidth of >60GHz at a bias voltage of –4V has been fabricated, and a tunable millimeter-wave source composed of an optical comb generator and this UTC-PD has been recently proposed [10]. Fig. (9) shows the RF output power dependence on the input light power. Saturation effects appear at input light power higher than 15dBm.

6. Conclusion

Presentation of high-speed photo-HBTs with optical cut-off frequencies higher than 100 GHz, optical gain higher than 30 dB, and optoelectronic integrated circuits, such as a narrow band amplifier at 28 GHz and upconversion mixers to the 28 and 42 GHz frequencies, developed at OPTO+, has been made. These results, added to those obtained by others laboratories [2,4,6], confirm the potentiality of the photo-HBT to integrate multifunctional photoreceivers for applications in high-speed communication systems. However, hitherto their impact on real systems has been relatively modest. One reason is that, in point-to-(multi)point optical systems, there is little need for more complex optoelectronic functionality as optoelectronic mixer or oscillators, and PIN/HBT photoreceivers have been a good compromise for applications up to 10-20Gb/s.

On the other hand, photodiodes with high-speed response and high saturation output can be used to greatly reduce the need for electronic preamplification, or even allow the decision circuit to be directly driven by the device. UTC-PD has shown to have excellent characteristics for this application, but top-illuminated photo-HBT based on a InP composite collector DHBT could draw both the separation of the absorption and drift regions with the interne amplifier effect to obtain higher responsivity and saturation output than photo-SHBT.

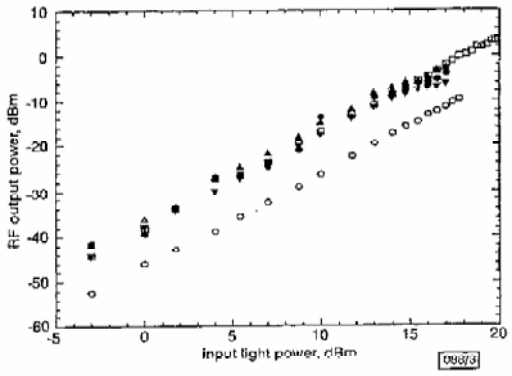

Fig. 3 *Output power dependence on input light power*

● 20 GHz
▲ 40 GHz
□ 60 GHz
▼ 80 GHz
○ 100 GHz

Fig. (9) Output power dependence on input light power of an OFCG/UTC-PD mm-wave source [10]

References

[1] J.C. Campbell and K. Ogawa, *J. Appl. Phys.*, 53(2) (1982) 1203-1208.

[2] Y. Betser et al., *J. Light. Tech.*, 16(4) (1998) 605-609.

[3] C. Gonzalez et al., Optoelectronic Up-converter to Millimetre-wave Band using a Heterojunction Bipolar Phototransistor", Proc. ECOC'98, vol. 1, pp. 443-444, 1998.

[4] H. Kamitsuna et al., *IEEE Trans. MTT*, 50(12) (2002) 3002-3007.

[5] M. Muller et al., *IEICE*, E86-C(7) (2003) 1299-1310.

[6] H. Kamitsuna et al., "A 82 GHz-Optical-gain-cutoff-frequency InP/InGaAs double-hetero-structure phototransistor (DHPT) and its application to a 40 GHz band OEMMIC photoreceiver", Proc. Of the European Microwave week 2000, EuMC36.

[7] D. Hiber et al., *J. Lightwave Techol.*, 18(7) (2000) 992-1000.
[8] D.C. Streit et al., "Indium Phosphide HEMT and HBT Production for Microwave and Millimeter-wave Applications", Proc. APMC2001, pp.9-14.
[9] N. Shimizu et al., *IEEE Photon. Technol. Lett.*, 10(3) (1998) 412-414.
[10] S. Fukushima et al., *Electron. Lett.*, 37 (2001) 780-781.

This article was reviewed at School of Applied Sciences, University of Technology, Baghdad, IRAQ

THE 2009 IAENG INTERNATIONAL CONFERENCE ON COMPUTER SCIENCE

19-21 March, 2009, Hong Kong

http://www.iaeng.org/IMECS2009/ICCS2009.html

The conference ICCS'09 is held under the International MultiConference of Engineers and Computer Scientists 2009. The IMECS 2009 is organized by the International Association of Engineers (IAENG), and serves as good platforms for the engineering community members to meet with each other and to exchange ideas. The last conference in 2008 has attracted a total of over one thousand participants from over 50 countries.

All submitted papers will be under peer review and accepted papers will be published in the conference proceeding. The abstracts will be indexed and available at major academic databases. The accepted papers will also be considered for publication in the special issues of the journal Engineering Letters, in IAENG journals and in edited books. Revised and expanded version of the selected papers may also be included as book chapters in the standalone edited books under the framework of cooperation between IAENG and Springer. For reference, the following IAENG post conference edited books, Trends in Intelligent Systems and Computer Engineering, Advances in Communication Systems and Electrical Engineering, and Advances in Industrial Engineering and Operations Research, have been published by Springer.

Important Dates:
Draft Manuscript submission deadline:
12 December, 2008
Camera-Ready papers & Pre-registration due:
10 January, 2009
ICCS 2009: **18-20 March, 2009**

Submission:
ICCS 2009 is now accepting manuscript submissions. Prospective authors are invited to submit their draft paper in full paper (any appropriate style) to **imecs@iaeng.org** by 12 December, 2008. The submitted file can be in MS Word format, PS format, or PDF formats.

The first page of the draft paper should include:
(1) Title of the paper;
(2) Name, affiliation and e-mail address for each author;
(3) A maximum of 5 keywords of the paper.

Also, the name of the conference that the paper is being submitted to should be stated in the email.

The topics of the ICCS'09 include, but not limited to, the following:
- **Theoretical computer science:**
- **Hardware:**
- **Computer systems organization:**
- **Computing methodologies:**
- **Computer applications:**

More details about the IMECS 2009 can be found at:
http://www.iaeng.org/IMECS2009/index.html

ISSN 1813-2065

Nobel Prize in Chemistry 2008

Prof. Osamu Shimomura, of Marine Biological Lab., Woods Hole, has won Nobel Prize in Chemistry 2008.
In 2006, we published Prof Shimomura's bestselling book on **BIOLUMINESCENCE: Chemical Principles and Methods**
This authoritative monograph provides a comprehensive overview of the biochemical aspects of all luminous organisms currently known and is invaluable to all researchers in the wonderful world of bioluminescence.

Coming CONFERENCE & SYMPOSIA

Sponsored & Organized by SPIE

IS&T/SPIE Electronic Imaging
Date(s): 18 – 22 January 2009
Location: San Jose, CA, USA

SPIE Photonics West
Date(s): 24 – 29 January 2009
Location: San Jose, California, USA
Exhibition: 27 – 29 January 2009

BiOS: Biomedical Optics
Date(s): 24 – 29 January 2009
Location: San Jose, CA, USA
Exhibition: 24 – 25 January 2009

LASE: Lasers and Applications
Date(s): 24 – 29 January 2009
Location: San Jose, CA, USA
Exhibition: 27 – 29 January 2009

MOEMS-MEMS: Micro and Nanofabrication
Date(s): 24 – 29 January 2009
Location: San Jose, CA, USA
Exhibition: 27 – 29 January 2009

OPTO: Integrated Optoelectronic Devices
Date(s): 24 – 29 January 2009
Location: San Jose, CA, USA
Exhibition: 27 – 29 January 2009

SPIE Medical Imaging
Date(s): 7 – 12 February 2009
Location: Orlando, Florida, USA
Exhibition: 9 – 11 February 2009

SPIE Advanced Lithography
Date(s): 22 – 27 February 2009
Location: San Jose, CA, USA
Exhibition: 24 – 25 February 2009

SPIE Smart Structures and Materials & Nondestructive Evaluation and Health Monitoring
Date(s): 8 – 12 March 2009
Location: San Diego, California, USA

Photomask and NGL Mask Technology XVI
Date(s): 8 – 10 April 2009
Location: Yokohama, Japan

SPIE Defense, Security, and Sensing
Date(s): 13 – 17 April 2009
Location: Orlando, FL, USA
Exhibition: 14 – 16 April 2009

SPIE Europe Optics and Optoelectronics
Date(s): 20 – 24 April 2009
Location: Prague, Czech Republic

ISPDI – International Symposium on Photoelectronic Detection and Imaging
Date(s): 1 – 5 May 2009
Location: Beijing, China

Microtechnologies for the New Millennium
Date(s): 4 – 6 May 2009
Location: Dresden, Germany

SPIE Scanning Microscopy 2009
Date(s): 4 – 7 May 2009
Location: Monterey, California, USA

SPIE Optifab
Date(s): 11 – 14 May 2009
Location: Rochester, New York, USA
Exhibition: 12 – 14 May 2009

International Photodynamic Association World Congress 2009
Date(s): 11 – 15 June 2009
Location: USA

SPIE Europe Optical Metrology
Date(s): 14 – 18 June 2009
Location: Munich, Germany

Optical Properties of Silicon Nanoparticles Produced by Nd:YAG Laser Ablation

Bassam G. Rasheed
Mohammed A. Ibrahem

School of Applied Sciences, University of Technology, Baghdad, IRAQ

Silicon nanoparticles films have been fabricated by laser ablation process using pulsed Nd:YAG laser. Various laser parameters were examined to produce films of different properties such as the laser energy, laser fluence, and the target-substrate distance. The experimental results have been fitted with the theoretical quantum confinement model to analyze the photoluminescence spectra and estimate the nanoparticle sizes and their distribution. From the optical transmission studies, we found that the band gap of the prepared nanostructured films was in the range (1.5-2.4)eV due to the existence of various nanoparticle sizes in the deposited film. Furthermore, the photoluminescence PL spectra indicate that the estimated band gap lies between (1.6-2.4)eV. While, the corresponding nanoparticle sizes contributing the PL emission were in the range (22-38)Å.

Keywords: Si nanoparticels, Laser ablation, Photoluminescence, Optical bandgap
Received: 6 August 2008, Revised: 9 September 2008, Accepted: 1 October 2008

1. Introduction

Silicon is an ubiquitous electronic material and the discovery of strong room temperature luminescence from porous Si in 1990 raised hopes it may find a new lease of life in the emerging field of optoelectronics [1]. Thereby, silicon nanocrystals have attracted considerable attention due to their potential applications for future nanoelectronic and especially optoelectronic devices [2,3]. Visible photoluminescence from porous silicon at room temperature triggered a world-wide research effort mainly aimed at investigating the possibilities to use silicon for optoelectronic applications like light emitting diode [4], modulators and solar cells due to the high surface area in addition to the fact which is, the nanostructured surface has a high refractive index therefore, this layer could be considered as an antireflection coating of solar cells [4-6]. Moreover, silicon nanostructures could also be employed in another areas like; biophysics, silicon based waveguides and nanotechnology [7,8].

One of the most direct effects of reducing the size of materials to the nanometer range is the appearance of quantization effects due to the confinement of the charge carriers. This will lead to discrete energy levels depending on the size of the structure as it is known from the simple potential well treated in introductory quantum mechanics [9]. Reducing dimensionality plays a major role in the behavior of the nanocrystalline system. In the case of nanocrystalline silicon, quantum confinement is dominant in transport processes and has an important contribution to the optical phenomena. Size quantization effects have two important characters. First, a change in the nature of the material band gap from indirect-toquasi direct. Second, an enlargement of the band gap, which leads to the efficient of the radiative recombination should account for an intense visible luminescence, which could result in a blue shift by reducing the sizes of the nanocrystallites [1,10]. The confinement of carriers on a low-dimensional semiconductor system is sensitive not only to the physical dimension but also to the shape of the confined volume [1]. The semiconductor nanostructure shows size dependent properties different from those of a macroscopic semiconductor if one or more dimensions of the structure are comparable to wavelength of light or wavelength of electrons and holes [5].

Silicon nanostructures could be produced by lasers in various methods such as laser induced etching [11-16], laser annealing [17-20] and laser ablation of silicon targets inside a vacuum chamber [21-25]. Each method could produce a nanostructure of specific features. Pulse laser deposition (PLD) by laser ablation has several advantages including the ability to produce materials with a complex stoichiometry and a narrower distribution of particle size, reduce porosity and control the level of impurities [8,26]. Despite its versatility and wide

ISSN 1813-2065

applicability, many aspects of the detailed physical process underlying the laser ablation suffer from lack of information on the structural properties of semiconductor nanoparticles deposited by PLD which is directly related to the principle of this deposition technique [27]. The major drawbacks of PLD are the occurrence of micron and nano-sized particles (droplets) in the deposited films which affects film quality and limits the applicability of characterization technique [8,27]. A seemingly esoteric of pulsed laser deposition has recently emerged as a potential methodology for growing nanostructures. It is as many characteristics, such as its ability to high-energy source particles, simple and nexpensive experimental setup [5]. This study aims to prepare silicon deposited film constituting silicon nanoparticles by the laser ablation process and study effects of various preparation parameters on the silicon nanoparticles sizes.

2. Experimental Setup

A pulsed Nd:YAG laser of 1-2.5J energy was employed to synthesize a nanostructured films by laser ablation of silicon target. Silicon nanoparticles films were deposited on a glass substrate under various preparation parameters such as laser energy, laser energy density and target-substrate distance. The deposition process was carried out under pressure of 5×10^{-4}torr at room temperature. The pulsed laser was focused on a rotating target to minimize a pit formation using quartz lenses mounted inside the vacuum chamber. The target mount was fixed at optimum angle of 45° with the incident laser pulse to reduce the interaction between the laser and evaporating material and to ensure that the optimum ejected particles reach the substrate. The laser-induced plasma plume expanded perpendicularly to the target surface and deposited on a glass substrate.

3. Results and Discussion

3.1 The optical band gap

It is well known that crystalline silicon has an indirect band gap, but in low dimensional silicon (silicon nanoparticles), the band gap is almost transferred to quasi direct [28,29]. Therefore, one could expect that for large sizes droplet (micron-sized particles), there is a probability for an indirect transition. We have also plotted the relation between the square absorption coefficient (α^2) with the optical band gap energy ($h\nu$) for films prepared by 40 pulses to estimate the optical band gap of the indirect transition.

A. Effect of laser energy

It was also found that the band gap energy is extremely affected by the incident laser energy. When low laser energy is incident on the target, a low number of large size silicon nanoparticles are ablated from the target and the estimated band gap energy was 1.75eV. Further increase in the laser energy leads to increase the laser power density and consequently the number of small nanoparticles and the corresponding band gap energy, as shown in Fig. (1).

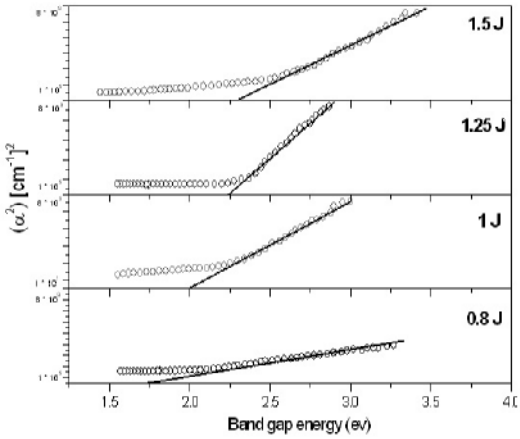

Fig. (1) The optical band gap to the samples prepared under different laser energies

This band gap reaches 2.3eV at higher laser energy as given in Table (1). More probably, the observed shift in the band-edge can be attributed to the decreasing in the particle size according to the quantum confinement effect.

Table (1) Effect of laser energy on the nanoparticles band gap

Laser energy (J)	Band gap (eV)
0.8	1.75
1	2
1.25	2.25
1.5	2.3

Similarly, we have also plotted the relation between ($\alpha^{1/2}$) and the band gap energy (right-hand y-axes in Fig. 2) to compare between the indirect band gap and direct band gap for the particles in the ablated film prepared by laser energy of 1.5J. It was found that the estimated indirect band gap has a smaller value (2.1eV) compared with that for direct band gap (2.3eV) and that is reasonable since the indirect band gap is shifted from the bulk value (1.12eV) to (2.1eV). In other words, the indirect band gap should take value closer to the bulk band gap [30].

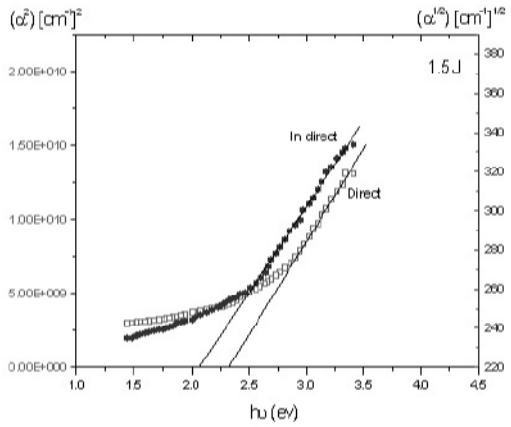

Fig. (2) The direct and indirect band gap to the film prepared at 1.5J

B. Effect of the laser fluence

Table (2) gives values of the energy band gap of the samples prepared under different laser fluences. The curves show shifts in the value of the band gap towards higher energy when increasing the laser fluence. This attributed to the decreases in the particle size with increasing laser fluence. This behavior can be explained by the quantum confinement model [31]. Increasing the laser fluence leads to efficient plume formation, therefore, the amount of vaporizing materials will increase. These materials are almost in the range of nanometer size. Moreover its band gap will be increase according to the quantum confinement effect. This result is consistent with Ref. [32].

Table (2) The optical band gap values to the samples prepared at different laser fluencies

Laser fluence (J/cm²)	Band gap (eV)
5	2
6	2.08
7	2.1
8	2.23

C- Effect of target-substrate distance

The band gap of the nanoparticles, measured from the optical absorption data at different target-substrate distances is given in Table (3). One can clearly see an increase in the band gap from 1.75eV to 2.3eV when the distance increases from 0.25cm to 0.5cm. On the other hand, increasing the target-substrate distance to 0.75cm leads to red shift of the band gap to 2.1eV since smaller-sizes nanoparticles have lighter weight and affected by the vacuum pressure inside the vacuum chamber and, subsequently, could not travel long distances to reach the substrate. This result is consistent with our results for the photoluminescence spectra, where the position of 0.5cm target-substrate distance produces smaller nanoparticle sizes and correspondingly larger band gap energy according to the quantum confinement model [33].

Table (3) The optical band gap at different target-substrate distances

Target-substrate distance (mm)	Band gap (eV)
2.5	1.75
5	2.3
7.5	2.1

3.2 The Photoluminescence (PL)

The quantum confinement model has been widely used by Suemoto *et al.* [34] and modified by Yorikawa *et al.* [35] to study the nanocrystallite size distributions in porous silicon from its photoluminescence spectra. According to the QC model, the emission wavelength and intensity depend on the nanocrystal diameter, size distribution and concentration. This model can explain the general tendency of most of the experimental results such as the blue-shift of the luminescence spectrum with a decrease of the silicon nanocrystallite (Si-nc) size. It is based on the fact that each nanoparticle in a porous silicon specimen contributes a characteristic sharp photoluminescence spectrum, where the total photoluminescence intensity $S(E)$ from an assembly of particles including size distribution is given by:

$$S(E) = c.\alpha(E_{extc.} - E).D(R_E).\frac{1}{n}.\frac{R_E}{E - E_g^o} \qquad (1)$$

where E is the gap energy of bulk silicon, c is a constant including an intensity of the light source of excitation energy ($E_{exc.}$), $\alpha(E_{exc.}-E)$ is the absorption coefficient as a function of energy, $D(R_E)$ is the size distribution function, n is the confinement parameter and R represents the crystallite radius

Photoluminescence (PL) spectra of silicon nanoparticle films prepared by ablating the silicon target with different laser fluence were studied with excitation laser source of 514nm (2.41eV) in order to ensure that widest range of particles sizes was excited. The photoluminescence spectra obtained from the experimental data have been fitted to spectra calculated by the quantum confinement model of electrons within dot particle structure as shown in Fig. (3).

The theoretical calculations are shown as continuous curves. As the laser fluence is increased from 4J/cm^2 to 7J/cm^2, the mean particles size decreases. For the sample prepared with 4J/cm^2, it was found that the FWHM=60meV with a standard deviation of σ=0.5Å, and the mean size of crystallites is L$_\circ$=38Å positioned at 1.6eV. For the sample prepared at 5J/cm^2, the photoluminescence peak intensity increases and shifted toward larger

energy which is about 1.7eV, while the FWHM was about 80meV, Fig. (3b). As the laser fluence is further increased to 6J/cm^2, the PL peak intensity is decreases as compared with the previous case and the FWHM is about 120meV, while the photoluminescence peak position is increased to 2.02eV and the crystallite size is L◦=26Å. The samples were produced at 7J/cm^2 laser fluence witness smaller particles size of about L◦=22Å and its FWHM is 130meV. One can clearly see that the crystallite size shifts towards smaller particles sizes with increasing laser fluence, because high laser fluence can supply more kinetic energy to the materials ejected during the deposition process.

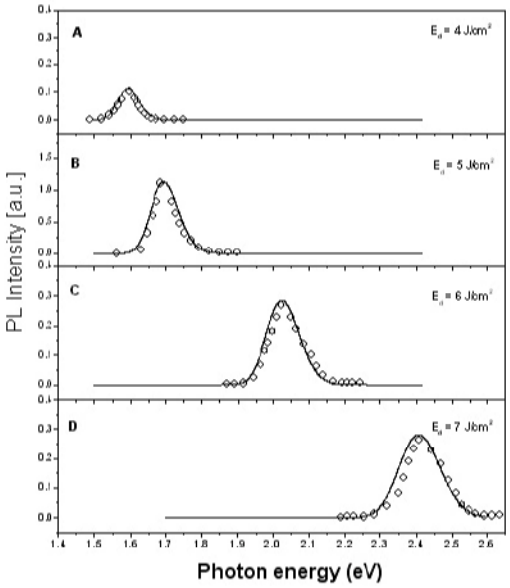

Fig. (3) PL spectra to the samples prepared at different laser fluences. The calculated results are represented in solid lines, while the experimental data are fitted in doted line

Also, it can be suggested that, when the laser fluence increased, the atoms mobility increases and this provides an appropriate condition for creating of smaller and denser silicon nanoparticle films. It should also be mentioned here that the photoluminescence intensity becomes higher for high laser fluence and that is due to the high number of small nanoparticles contributing the emission.

4. Conclusions

Optical properties of silicon nanostructure films have been investigated as a function of laser energy, target-substrate distance and laser energy density, in order to realize the effect of these experimental conditions on the optical properties of the produced Si films. It was found that the nanostructured films have interesting and unique optical properties. Due to the nanoparticle size distribution in the deposited films, the average value of the band gap is affected by different preparation conditions. From the optical transmission spectra of the deposited films, it is found that the band gap increases with increasing the laser energy and the laser fluence according to the quantum confinement effect. Laser ablation of silicon offers an excellent technique to produce silicon nanoparticles due to the following features: good size control, efficient luminescence through quantum dot structure and selective absorption properties.

References

[1] B.G. Rasheed, "Spectroscopy of Porous Silicon Prepared by Laser Induced Etching", Ph.D. Thesis, Department of Physics, Indian Institute of Technology, Delhi, India (2001).
[2] T. Qiu et al., *J. Cryst.Growth*, 277 (2005) 143-148.
[3] H.S. Mavi et al., *J. Noncryst. Sol.*, 286 (2001) 162-168.
[4] A. Irrara, "Light Emitting Devices Based on Silicon Nanostructures", Ph.D. Thesis, Department of Physics, University of Deglistudidi Catania, Italy, 29 (2004).
[5] L.M. Kukreja, B.N. Singh and P. Misra, Pat. (CAT), Indore, INDIA (2006).
[6] A.F. Mohammed, "Study of Laser Effects on Porous Silicon Properties", M.Sc. Thesis, School of Applied Sciences, University of Technology, Baghdad, Iraq (2006).
[7] P.R. Willmott and J.R. Huber, *Rev. Mod. Phys.*, 72 (2000) 1.
[8] M.H. Wu et al., *Mater. Sci. Eng. B*, 5 (2005) 273-277.
[9] K. Pederson, "Quantum size effects in nanostructures", Ph.D. Thesis, Department of Physics and Nanoscience, Alborge University, Denmark (2006).
[10] J.H. Kim et al., *Thin Solid Films*, 41 (2002) 4.
[11] R. Kumar, H.S. Mavi and A.K. Shukla, *Thin Solid Films*, 34 (2007) 1-7.
[12] Y. Zhao et al., *J. Of Lumen.*, 128 (2008) 317-320.
[13] H.S. Mavi et al., *Mater. Sci. Eng. B*, 97 (2003) 239-244.
[14] M.R. Hashim and K.Q. Salih, *Mic. Elec. Eng.*, 81 (2005) 243-250.
[15] S. Aravamudhan et al., Appl. Phys. A, 87 (2007) 773-780.
[16] H. Khalili et al., *J. Mater. Sci.*, 42 (2007) 908-913.
[17] X. Li et al., *Sol. Stat. Phenom.*, 121 (2007) 33-36.
[18] A. Tewary, R.D. Kekatpure and M.L. Brongersma, *Appl. Phys. Lett.*, 88 (2006) 353-359.
[19] N. Misra et al., *Appl. Phys. Lett.*, 90 (2007) 111111.

[20] I. Avrutsky et al., D. G. Georgiev, D. Frankstein, G. Auner, G. Newaz, Appl. Phys. Lett., 84 (2004) 13.
[21] Y. Wang, W. Xu, Y. Zhou, L. Chu, G. Fu, *Laser and Particle Beams*, 25 (2007) 9-13.
[22] N.G. Semaltianos et al., Mater. Lett. 56 (2007) 1-6.
[23] L. Cultrera et al., *Appl. Phys. A*, 88 (2007) 435-437.
[24] Y.L. Wang et al., *Thin Solid Films*, 515 (2006) 1897-1900.
[25] W.R. Harp, J.R. Dilwith and J.F. Tu, *J. Mater. Proc. Tech.*, 198 (2008) 22-30.
[26] S. Eliezer et al., *Phys. Rev. B*, 69 (2004) 144119.
[27] D. Riabinina, F. Rosei and M. Chaker, *J. Nanoscience*, 1(1) (2005) 83-89.
[28] K.V. Narasimham et al., *Infrared Physics*, 23(6) (1983) 349-353.
[29] W.W. Scanlon, *Phys. Rev. B*, 109 (1958) 1.
[30] J.I. Pankove, **"Optical Process in Semiconductors"**, David Sarnoff Research Center, Englewood Cliffs, New Jersey (1971).
[31] L.T. Canham, *Appl. Phys. Lett.*, 57(10) (1990) 1046.
[32] A. Malinin, S. Novikov, V. Ovchinnikov, et al., Reports in Electron Physics, Department of Electrical and Communications Engineering, University of Technology, Helsiniki, (2001).
[33] L. Canham, **"Properties of Porous Silicon"**, EMIS, Data Reviews Series, 18, London (UK) (1997).
[34] T. Suemoto et al., *Phys. Rev. Lett.*, 70 (1993) 3659.
[35] H. Yorikawa and S. Muramatsu, *Appl. Phys. Lett.*, 644 (1997) 644.

This article was reviewed at Physics Department, Research Institute of Science and Technology (POSTECH), Namku Pohang, KOREA, and School of Applied Sciences, University of Technology, Baghdad, IRAQ

 ISSN 1813-2065

Coming

CONFERENCES & SYMPOSIA

Sponsored & Organized by Institute of Physics (IOP)

Advanced Measurement Techniques in Tribology
15 October 2008
Institute of Physics, London, UK
Organised by: the Tribology Group of the Institute of Physics

Sustainable Energy: New Solutions from Physics and Engineering
29 October 2008
Institute of Physics, London, UK
Organised by: the Applied Physics and Technology Division of the Institute of Physics

Preparation and Patterning of Magnetic Materials
4 November 2008
Institute of Physics, London, UK
Organised by: the Magnetism Group of the Institute of Physics

Experimental techniques in Semiconductor Research
19 November 2008
East Midlands Conference Centre, Nottingham, UK
Organised by : the Semiconductor Physics Group of the Institute of Physics

Low Temperature Techniques Course
26 November 2008
East Midlands Conference Centre, Nottingham, UK
Organised by : the Low Temperature Group of the Institute of Physics

BRSG Christmas Meeting 2008
10 December 2008
Institute of Physics, London, UK
Organised by : the BRSG Group of the Institute of Physics

Imaging to Understanding: Insight Through Visualisation
17 – 18 December 2008
Village Hotel, Nottingham, UK
Organised by: the Conferences Strategy Committee of the Institute of Physics

A Random Walk Through Polymer Science
19 December 2008
Institute of Physics, London, UK
Organised by : the Polymer Physics Group of the Institute of Physics

17th Interdisciplinary Surface Science Conference (ISSC 17)
30 March – 02 April 2009
University of Reading, Reading, UK
Organised by: the Thin Films and Surfaces Group of the Institute of Physics

Biological and Soft Matter
6 – 8 April 2009
University of Warwick, UK
Organised by: the Biological Physics, Liquids and Complex Fluids and Polymer Physics Groups of the Institute of Physics

Dielectrics 2009
15 – 17 April 2009
University of Reading, UK
Organised by: the Dielectrics Group of the Institute of Physics

Fourth International Conference on Conservation and Preservation Issues Related to Digital Printing
20 – 21 April 2009
Institute of Physics, London, UK
Organised by: the Printing and Graphics Science Group of the Institute of Physics

Gianfranco Cerofolini
Dario Narducci
Paolo Amato
Elisabetta Romano*

CNISM and Department of Materials Science, University of Milano–Bicocca, 20125 Milano MI, ITALY

Fractal Nanotechnology (Invited Paper)

Self-similar patterns are frequently observed in Nature. Their reproduction is possible on a length scale 10^2–10^5 nm with lithographic methods, but seems impossible on the nanometer length scale. It is shown that this goal may be achieved via a multiplicative variant of the multi-spacer patterning technology, in this way permitting the controlled preparation of fractal surfaces.

Keywords: Spacer technology, Sub-lithographic preparation, Fractals
Received: 10 October 2008, Accepted: 18 October 2008

1. Introduction

Nanotechnology is essentially related to the problems of (1) predicting the properties of matter on the nanometer length scale, (2) preparing samples with accurately controlled size on that length scale, and (3) making accessible such samples to the macroscopic world. The first problem is essentially related to the fact that the nanoscale is characterized by the so called $(N+1)$ problem: the properties of a system with N particles may be largely different from those of a system with $(N+1)$ particles [1]. The preparation of nanoscopic samples with assigned properties requires therefore an extreme accuracy in the preparation.

The master road for the reproducible preparation of bodies in planar arrangement with assigned shape is photolithography. This technique has been able to produce features with progressively scaled size, the currently producible feature size being of several tens of nanometers. This size reduction, however, has been possible only thanks to the development of apparatuses of either huge economic cost (extreme ultraviolet lithography) or very low throughput (electron beam lithography).

In recent years, however, techniques not involving the use of advanced lithography have been developed for the preparation of nanometer-sized features. The most advanced ones are based on the transformation of vertical features into horizontal features and allow the preparation of lines with controlled width of 10–20 nm. Although this strategy allows the preparation of simple geometries only (line arrays), the development of new architectures [2] makes up for this inherent limitation. Among them the crossbar structure is particularly attractive [3-5] because it may simply be produced by crossing two perpendicularly oriented wire arrays and each cross-point may be functionalized with the insertion of suitable molecules [6].

The first method for the non-lithographic preparation of ultra-dense line arrays was originally proposed by Natelson et al. [7]. It is essentially based on the sequential alternate deposition of two films A and B characterized by the existence of a preferential etch for one of them (say, A). After cutting at 90°, polishing, and controlled etching of A, one eventually gets a mold that can be used as a mask for imprint lithography (IL). Actually IL is a *contact* (rather than proximity) lithography; what is non-lithographic is uniquely the way used for the preparation of the mask. The first practical application of this idea was provided by Melosh et al. [8] who prepared a contact mask for IL with pitch of 16 nm by growing on a substrate a quantum well via molecular beam epitaxy, cutting the sample perpendicularly to the surface, polishing the newly exposed surface, and etching selectively the different strata of the well.

Another route for the non-lithographic preparation of ultra-dense line arrays is the multi-spacer patterning technique (S^nPT). This technology was developed by Cerofolini et al. [9,10] with the goal of producing wire arrays with pitch on the nanometer length scale exploiting the already existing CMOS (complementary metal-oxide-semiconductor) IC (integrated circuit) technology only. In this way the S^nPT may be viewed as a conservative extension of the current IC technology to the nanoscale length scale [11]. In the original formulation of S^nPT (hereinafter referred to as 'additive route', S^nPT_+) an array of $2n$ bars is directly defined onto a substrate via a sequence of n conformal depositions and anisotropic etchings. This idea is just an extension of the spacer patterning technique (SPT), conventionally used in microelectronics for the self-alignment of the gate electrode on source-and-drain regions [12]. The density limit of crossbars prepared using S^nPT_+ are discussed in Ref. [13]: although cross-point density of 8×10^{10} could be achieved within the current technology, the overall process would however require 20 repetitions of each SPT cycle.

ISSN 1813-2065

2. Multiplicative Route

Managing so many deposition-etching cycles may however be difficult and expensive. Observing that the SPT allows, starting from one seed, the preparation of *two* spacers, the above difficulty may be removed using a *multiplicative* variant (referred to as $S^nPT_\times$) of the multi-spacer patterning technique.

$S^nPT_\times$ requires that each newly grown spacer is used as seed for the subsequent growth – that is possible if the original seed is etched away at the end of any cycle. In $S^nPT_\times$ each multiplicative $SPT_\times$ cycle involves therefore the following steps:

The conformal deposition of a film on an assigned seed of high aspect ratio,

(ii) Anisotropic etching of the film down to the appearance of the original seed, and

(iii) The selective etching of the seed.

Figure (1) sketches two $SPT_\times$ repetitions and shows that the material nature changes on going from one set of spacers to the subsequent one, so that the spacer material alternates, in our preferred embodiment, between poly-silicon and SiO_2. Since the wire material is poly-silicon, the material of the first deposited layer depends on the parity of n: if n is even, it should be in SiO_2; otherwise in poly-silicon.

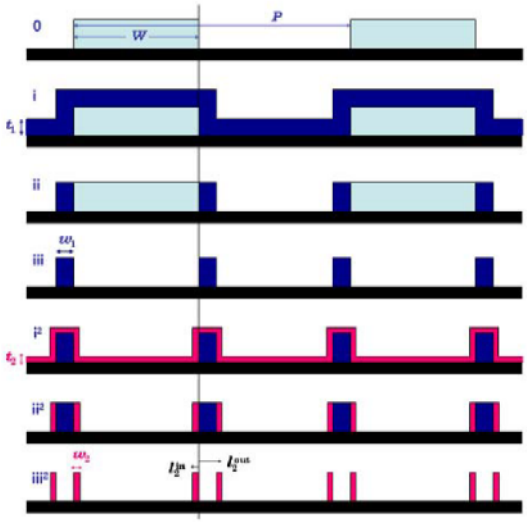

Fig. (1) Two steps for the formation of a sub-lithographic wire array starting from a lithographic seed array

The figure, however is highly idealized and does not show that, due to unavoidable side effects, the eight of the spacer at a given stage is lower than that at the previous stage [13]; previous studies have shown that the spacer height t_n decreases from the height of the lithographic seed t_0 almost linearly with n,

$$t_n = t_0 - n\tau \qquad (1)$$

with τ being the height loss per $SPT_\times$ cycle; τ depends on how accurately the technology has been set.

The first demonstrators of $S^nPT_\times$ for the generation of gratings sub-lithographic pitch go back to more than a score of years [14]; the usefulness of this technique for the preparation of wire arrays potentially useful for biochips, instead, is much more recent [15].

Let P and W denote the lithographic pitch and wire width, respectively; P is determined by the considered lithographic technology while W may be varied almost at will controlling exposure, etching, etc. As discussed in Ref. [13], the maximum density is however achieved taking

$$P = 3W \qquad (2)$$

and depositing on the bar of width w_{n-1} a conformal film of thickness s_n given by

$$s_n = \frac{1}{2} w_{n-1} = \frac{1}{2} s_{n-1}, \text{ so that}$$

$$w_n = s_n = \frac{1}{2^n} W \qquad (3)$$

While the repetition in additive way of n SPTs per (bottom and top) layers magnifies the lithographically achievable cross-point density by a factor of $(2n)^2$, the repetition in a multiplicative way gives a magnification of 2^{2n}.

This matter is discussed thoroughly in another paper [13]; rather, in this work we intend to discuss another property of $S^nPT_\times$—the possibility of preparing self-similar features with sub-lithographic definition.

3. The Multiplicative Route as a Technique for the Generation of Fractal Structures

Imagine for a moment that, in spite of the atomistic nature of matter and of the inherent technological difficulties, the multiplicative route can be repeated indefinitely. Remembering that the $(n + 1)$-th step generates a set S_{n+1} that is nothing but the one at the n-th, S_n, at a lower scale, the sequence $\{S_0, \ldots, S_n, \ldots\}$ defines a fractal; it will be referred to as multi-space set fractal. Assuming the scaling law above [Eq. (3)], this fractal is self-similar only if the height of each spacer varies with n as 2^{-n}. Otherwise, if the structure scales only in one dimension or if its height scales with different law than in (Eq. (3)), the fractal is self-affine [16]. As mentioned above, the 'spontaneous' height decreases with n (Eq. (1)) renders the fractal self-affine. A self-similar fractal can be obtained at the end of process planarizing the whole structure with a resist and sputter etching in a non-selective way the composite film until the thickness is reduced to $t_0/2^n$.

It is however noted that even ignoring the technological factors, the atomistic structure of matter limits the above considerations to an interval of 1–2 orders of magnitude, ranging from few atomic layers to the lower limits of standard lithography.

Having clarified in which limits the set S_n may be considered a fractal, it is interesting to compare it with other fractal sets. The prototype of such sets, and certainly the most interesting from the speculative point of view, is certainly the Cantor middle-third excluded set. Figure (2) compares sequences of three discrete processes eventually leading to the multi-spacer fractal set ***S*** and to the Cantor set ***C***. The comparison shows interesting analogies: Take $P = 2W$; if $w_n = \frac{1}{3} W_{n-1}$ the measure of each multi-fractal-step set coincides with that of the Cantor-step set. This implies that the multi-spacer fractal set has null measure. Similarly, it can be argued that the multi-spacer set, considered as a subset of the unit interval, has the same fractal dimension as the Cantor middle – third excluded set – ln(2)/ln(3) [16].

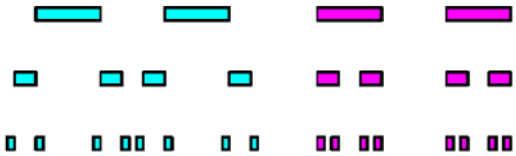

Fig. (2) Generation of the multi-spacer set (left) and of the Cantor middle-third excluded set (right)

At each step the multi-spacer fractal set is characterized by a more uniform distribution of single intervals than the Cantor set; this makes the former more interesting for potential applications than the latter. In spite of that, trying to reproduce the Cantor set on the nanometer length scale seems of a certain interest. This is possible with existing technologies; as shown in Fig. (3), the process involves

(C1) the lithographic definition of seed (formed, for instance, by poly-silicon) generating the Cantor set,

(C2) its planarization (for instance, via the deposition of a low viscosity glass and its reflow upon heating),

(C3) the etching of this film to a thickness controlled by the exposure of the original seed,

(C4) the selective etching of the original film,

(C5) the conformal deposition of a film of the same material as the original seed (poly-silicon, in the considered example) and of thickness equal to 1/3 of its width,

(C6) its anisotropic etching, and

(C7) the selective etching of the space seed (glass, in the considered example).

Although the preparation of fractal structures may appear at a first sight nothing but a mere exercise of technology stressing, in the following we discuss some of their possible applications: (1) Systems biology, i.e. the study of the complex interactions in biological systems, is now overcoming the limits of molecular biology. Systems biology requires the knowledge of the cellular state at subcellular level (single constituting organelles: mitochondria, ribosomes, etc.).

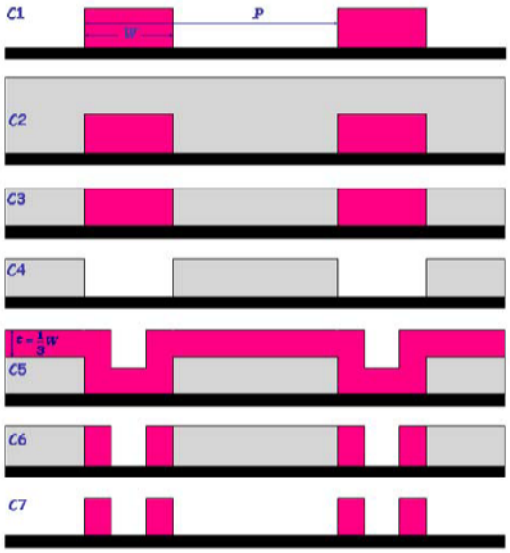

Fig. (3) A process for the generation of Cantor middle-third excluded set

Sensing at this level, with space resolution in the deep sub-micrometer region, is impossible with CMOS devices, defined lithographically. Several attempts to overcome the CMOS limits are known [17,18]; fractal technology, being able to transform a smart lithographic pattern (i.e. designed to the wanted function) in itself at a much lower scale, seems suitable for such a purpose. In particular, a matrix formed by the Cartesian product of two Cantor sets [16] would have next-to-nothing contact area, thus providing sensing with minimum perturbation. (2) Super-hydrophobic surfaces may be prepared controlling roughness and surface tension of non-wetting surfaces [19-21]. Whereas surface tension is a material property, roughness can be controlled by the preparation. For instance, roughness may be imparted depositing a suitable relief on the surface. In this way, however, an amount of area is lost for other application. Although it is possible that the control of wetting properties does not require to manage geometries on the nanoscale, this loss may be minimized designing the relief in such a way as to have almost nil area (as in the example above). (3) If the S ^{n} PT is used for the preparation of crossbar structures for molecular electronics, the functionalization with organic molecules of the cross-points can only be done after the preparation of the hosting structure. According to the analysis of Ref. [22], this requires an accurate control of the rheological and diffusion properties in a medium embedded in a domain of complex geometry. Understanding how such

properties change when the size is scaled and clarifying to which extent the domain can indeed be viewed as a fractal (so allowing the analysis on fractals [23] to be used for their description) may be a key point for the actual exploitation of already producible nanometer-sized wire arrays in molecular electronics.

4. Discussion

Figure (4) shows in plan view a comparison between the following crossbars:
(a) a 2×2 crossbar obtained by crossing lithographically defined lines;
(b) a 16×16 crossbar obtained via S^8PT_+ starting from lithographically defined seeds separated by a distance allowing the optimal arrangement of the wire arrays;
I a 16×16 crossbar obtained via $S^3PT_\times$ starting from lithographically defined seeds separated by a distance satisfying Eq. (2), and
(d) a 16×16 crossbar obtained via $S^3PT_\times$ starting from lithographically defined seeds and arranging the process to generate the Cantor middle-third excluded set.

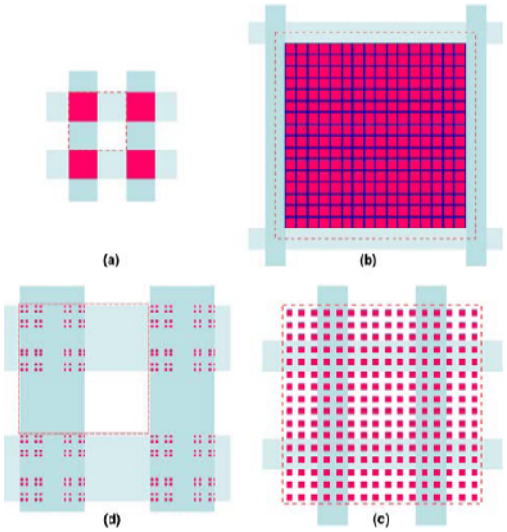

Fig. (4) Plan-view comparison of the crossbars obtained (a) crossing lithographically defined lines, (b) using the lithographically defined lines above as seeds for S^8PT_+, (c) using the lithographically defined lines above as seeds for $S^3PT_\times$, and (d) a Cantor middle-third excluded set using a minor variant of $S^3PT_\times$. In each structure the square with dashed sides denotes a unit cell suitable for the complete surface tiling

The figure has been drawn in the following hypotheses:
1. The lithographic lines in (a) and (b) have width at the current limit for large-volume production, say W=65nm;
2. The height loss τ is such that the maximum number of repetitions in the additive route is 8, and the sub-lithographic pitch is the same as reported in Refs. [9,10]; and

The lithographic width of I is chosen to allow the minimum pitch to be consistent with the one obtained with the additive route (W = 100 nm), in this way producing sub-lithographic wires with width (12.5nm) that has been proved to be producible [15].
Figure (4) shows that the multiplicative route succeeds in producing crossbars with cross-point density comparable with that achieved with the additive route, however, using a remarkable smaller number of SPT repetitions. To estimate the advantage of $S^n PT_\times$ over $S^n PT_+$, consider for instance the case of the repetition of three $SPT_\times$ per layer. This would produce a magnification of the lithographic cross-point density by a factor of $2^3\times2^3$. Taking W=0.1μm, after 3 $SPT_\times$ repetitions the spacer width should be of 12.5nm, with minimum separation of 25nm. Taking into account Eq. (2), the cross-point density achievable with the repetition of 2×3 $SPT_\times$ would thus be nearly the same as that obtainable with the repetition of 2 × 8 SPT_+.

5. Conclusions

Some fractals (Cantor set, Peano and Koch curves, etc.) were known in mathematics well before the construction of a comprehensive theory [16]. Actually, the theory of fractals affirmed as such that only after Mandelbrot observation many physical phenomena can be described, although approximately and on a limited length scale, as fractals [24].

The usefulness of fractal algorithm is well known: assuming that human hairpins can be described, at least approximately as fractals, the use of fractal generator, rather than of the whole image, would greatly simplify storage and transmission of the corresponding image.

That real systems may be pictured as fractal set on the nanometer (and thus microscopic) length scale was first demonstrated by the analysis by Avnir, Farin and Pfeifer for the surfaces of several porous adsorbents [25-27]. In this work we have shown that the multiplicative route of the multi-spacer patterning technique allows the preparation of ordered fractals on the mesoscopic length scale.

Although at this stage we have no ideas of the possible practical applications of fractal technology, we nonetheless believe that the possibility of preparing, without the use of advanced lithography, fractal structures at the mesoscopic scale opens a virgin field of applications. The above considerations are certainly highly speculative, but not so speculative as those contained in van Gulick's paper in topochemistry [28], outlining applications currently not achievable at that time, but later demonstrated to be possible.

References

[1] A.M. Stoneham, *Mater. Sci. Eng.*, C 23 (2003) 235.
[2] M. Forshaw et al., *Nanotechnology,* 23 (2004) S220.
[3] J.R. Heath et al., *Science,* 280 (1998) 1716.
[4] K.K. Likharev, in *Nano and Giga Challenges in Microelectronics*, ed. By J. Greer, A. Korkin, J. Labanowsky (Elsevier, Amsterdam, 2003)
[5] P.J. Kuekes, D.R. Stewart and R.S. Williams, *J. Appl. Phys.*, 97 (2005) 034301.
[6] G.F. Cerofolini, *Appl. Phys.*, A 86 (2007) 31.
[7] D. Natelson et al., *Appl. Phys. Lett.*, 77 (2000) 1991.
[8] N.A. Melosh et al., *Heath, Science*, 300 (2003) 112.
[9] G.F. Cerofolini et al., *Microelectr. Eng.*, 81 (2005) 405.
[10] G.F. Cerofolini et al., *Nanotechnology,* 16 (2005) 1040.
[11] G.F. Cerofolini, *Nanotechnol. E-Newslett.*, 7 (2005) 5.
[12] W.R. Hunter et al., *IEEE Electron Device Lett.*, 2 (1981) 4.
[13] G.F. Cerofolini, P. Amato and E. Romano, *Semicond. Sci. Technol.*, 23 (2008) 075020.
[14] D.C. Flanders and N.N. Efremow, *J. Vac. Sci. Technol.*, B 1 (1983) 1105.
[15] Y.-K. Choi et al., *J. Vac. Sci. Technol.*, 21 (2003) 2951.
[16] K. Falconer, **"Fractal Geometry: Mathematical Foundations and Applications"**, Wiley (New York) (2003).
[17] L. Hood et al., *Science,* 306 (2004) 640.
[18] E. Stern et al., *Nature,* 445 (2007) 519.
[19] R.N. Wenzel, *Ind. Eng. Chem.*, 28 (1936) 988.
[20] A.B.D. Cassie and S. Baxter, *Trans. Faraday Soc.*, 40 (144) 546.
[21] A. Tuteja et al., *Science,* 318 (2007) 1618.
[22] G.F. Cerofolini et al., *Semicond. Sci. Technol.*, 22 (2007) 1053.
[23] J. Kigami, **"Analysis on Fractals"**, Cambridge Univ. Press (Cambridge) (2001).
[24] B.B. Mandelbrot, **"The Fractal Geometry of Nature"**, Freeman (New York) (1982).
[25] P. Pfeifer and D. Avnir, *J. Chem. Phys.*, 79 (1983) 3558.
[26] D. Avnir, D. Farin and P. Pfeifer, *J. Chem. Phys.*, 79 (1983) 3566.
[27] D. Avnir, D. Farin and P. Pfeifer, *Nature,* 308 (1984) 261.
[28] N. Van Gulick, *New J. Chem.*, 17 (1993) 619.

This article was reviewed at School of Applied Sciences, University of Technology, Baghdad, IRAQ

ISSN 1813-2065

CFP: IAENG International Conference on Computer Science ICCS 2009

19-21 March, 2009, Hong Kong
http://www.iaeng.org/IMECS2009/ICCS2009.html

The conference ICCS'09 is held under the International Multi-Conference of Engineers and Computer Scientists 2009. The IMECS 2009 is organized by the International Association of Engineers (IAENG), and serves as good platforms for the engineering community members to meet with each other and to exchange ideas. The last conference in 2008 has attracted a total of over one thousand participants from over 50 countries.

All submitted papers will be under peer review and accepted papers will be published in the conference proceeding (ISBN: 978-988-17012-2-0). The abstracts will be indexed and available at major academic databases. The accepted papers will also be considered for publication in the special issues of the journal Engineering Letters, in IAENG journals and in edited books. Revised and expanded version of the selected papers may also be included as book chapters in the standalone edited books under the framework of cooperation between IAENG and Springer. For reference, the following IAENG post conference edited books, Trends in Intelligent Systems and Computer Engineering, Advances in Communication Systems and Electrical Engineering, and Advances in Industrial Engineering and Operations Research, have been published by Springer.

Important Dates:
Draft Manuscript submission deadline: 12 December, 2008
Camera-Ready papers & Pre-registration due: 10 January, 2009
ICCS 2009: 18-20 March, 2009

Submission:
ICCS 2009 is now accepting manuscript submissions. Prospective authors are invited to submit their draft paper in full paper (any appropriate style) to imecs{at}iaeng.org by 12 December, 2008. The submitted file can be in MS Word format, PS format, or PDF formats.
The first page of the draft paper should include:
(1) Title of the paper;
(2) Name, affiliation and e-mail address for each author;
(3) A maximum of 5 keywords of the paper.
Also, the name of the conference that the paper is being submitted to should be stated in the email.

The topics of the ICCS'09 include, but not limited to, the following:

Theoretical computer science:
Algorithmic information theory
Computability theory
Cryptography
Formal semantics
Theory of computation
Analysis of algorithms and problem complexity
Logics and meanings of programs
Mathematical logic and Formal languages
Type theory

Hardware:
Control structures and Microprogramming
Arithmetic and Logic structures
Memory structures
Input/output and Data communications
Logic Design
Integrated circuits
VLSI design
Performance and reliability

Computer systems organization:
Computer architecture
Computer networks
Distributed computing
Performance of systems
Computer system implementation

Computing methodologies:
Symbolic and Algebraic manipulation
Artificial intelligence
Computer graphics
Image processing and computer vision
Pattern recognition
Speech recognition
Simulation and Modeling
Document and text processing
Digital signal processing

Computer applications:
Administrative data processing
Enterprise resource planning
Customer relationship management
Human Resource Management Systems
Mathematical software
Numerical analysis
Automated theorem proving
Computer algebra systems
Physical science and Engineering
Computational chemistry
Computational physics
Life and medical sciences
Bioinformatics
Computational biology
Medical informatics
Social and behavioral sciences
Computer-aided engineering
Robotics
Human-computer interaction
Speech synthesis
Usability engineering
Telecommunications
Queueing theory

More details about the IMECS 2009 can be found at:
http://www.iaeng.org/IMECS2009/index.html

More details about the International Association of Engineers, the journal Engineering Letters and the IAENG International Journal of Computer Science can be found at:
http://www.iaeng.org/about_IAENG.html
http://www.engineeringletters.com
http://www.iaeng.org/IJCS/index.html

****

Preparation and Characterization of Self-Assembled n-ZnS Thin Films

Charita Mehta
Jasim M. Abbas
G. S. S. Saini
S. K. Tripathi

Department of Physics, Centre of Advanced Study in Physics, Panjab University, Chandigarh–160 014, INDIA

We have synthesized ZnS nano-crystalline (n-ZnS) powder using zinc acetate and thiourea from chemical route at different pH. The average crystal size is determined as 3-5 nm with the help of X-ray diffraction. The formation of ZnS has been confirmed with the help of infrared (IR) spectroscopy by observing bands corresponding to the multi phonon absorption. IR spectrum also confirms presence of the capping agent on ZnS. Thin films of ZnS have also been deposited on glass and quartz substrates from the solution using self-aggregation approach. Refractive index (n) of the films is also determined. The optical band gap is calculated from the Tauc's extrapolation and is found to be dependent on pH of the bath solution. Electrical conductivity measurements have been done on these thin films and the activation energy has been calculated.

Keywords: n-ZnS, Nanocrystalline powder, Self-assembling, Optical band gap
Received: 11 July 2008, Revised: 2 October 2008, Accepted: 9 October 2008

1. Introduction

In recent years, properties of nanosized materials have generated a great deal of interest because of the science involved in these studies and technological applications of these materials. As the physical dimensions of the particle approach to the nanometer scales, quantization and surface effects begin to play an important role, leading to drastic changes in the measured properties [1]. Semiconductor nanoparticles have attracted much attention because of their novel electric and optical properties originating from surface and quantum confinement effects [2-5]. ZnS is a II-VI semi conducting material with a wide direct band gap of 3.65eV in the bulk. It has potential applications in optoelectronic devices such as blue light emitting diodes [6], electroluminescence devices and photovoltaic cells which enable wide applications in the field of displays [7-8], sensors and lasers [9]. In recent years, nanocrystalline ZnS attracted much attention because the properties in nanoforms differ significantly from those of their bulk counterparts. Therefore, much effort has been made to control the size, morphology and polycrystallinity of the ZnS nanocrystals with a view to tune their physical properties. Hence, there has been growing interest in developing techniques for preparing semiconductor nanoparticles and films. The wet chemical synthesis method is a simple and inexpensive alternative to more complex chemical vapor deposition (CVD) and physical techniques. The physical methods [10], which are commonly used for the fabrication of nanomaterials, have some resolution limits that restrict these techniques from reaching the nanometer scale. On the other hand, the wet chemical technique offers a simple means to synthesize such particle with good control of size and size distribution [11]. Therefore, the authors have decided tp prepare the n-ZnS powder and thin films with varying deposition parameter such as pH of the bath solution. Section 2 describes the experimental details. The results have been presented and discussed in section 3. The last section deals with the conclusion of this work.

2. Experiment

We have synthesized ZnS nano-crystalline powder from chemical route at different pH (=7, 10, 12) with capping agent (tri-sodium citrate). Aqueous solution of ZnS has been prepared by dissolving a nominal amount of zinc-acetate, capping agent (tri-sodium citrate) and thiourea for sulfide ion source in 50 ml deionized water and the resultant mixture has been stirred at elevated temperature. The solid phase is isolated by filtration and finally dried in hot bath, from the residue solution. This solid phase consists of ZnS nano-crystals. Thin films have been deposited on cleaned glass, quartz substrates and KBr pallets for the optical, electrical and structural measurements.

Crystallographic study has been carried out using a Phillips PW-1610 X-ray diffractometer

ISSN 1813-2065

using CuK_α radiation in the 2θ range from 10° to 70°. The IR spectrum is determined on a Perkin-Elmer PE-Rx 1 FTIR spectrophotometer. The spectral resolution of the IR spectrophotometer was 1 cm^{-1} throughout the experiment. To study the optical properties of n-ZnS thin films, the transmission spectra are recorded using a double beam UV/VIS/NIR spectrometer [Hitachi-330] in the transmission range 300-1000 nm for all samples. The electrical measurements of these thin films were carried out in a specially designed metallic sample holder. A vacuum of about 10^{-3}mbar is maintained throughout these measurements. Planar geometry of the films (length ~1.0cm; electrode gap ~8×10^{-2}cm) is used for the electrical measurements. Thick In electrodes were used for the electrical contacts. Thickness of the film is measured as ~615nm with a profile meter. The electrical conductivity is noted manually from a digital picoammeter (DPM-11 Model). The accuracy in current measurements is typically 1pA.

3. Results and Discussion

3.1 Optical Properties

Fig. (1) shows the XRD pattern of n-ZnS film deposited on the glass substrates (pH=12). The spectrum in Fig. (1) shows the diffraction peaks at 2θ values of 29.5°, 48.7° and 57.5° on the film deposited at pH=12. The highest intensity reflection peak is at 2θ=29.5° [111], with two another small intensity peaks at 2θ=48.7° [220] and 57.5° [311] indicating that [111] is the preferred direction. The intensity of these peaks increases as the pH value decreases (results not shown here). The comparison of observed `d' values with standard `d' values [12,13] confirms the sphalerite cubic (zinc blende type) nanocrystalline structure of ZnS thin films.

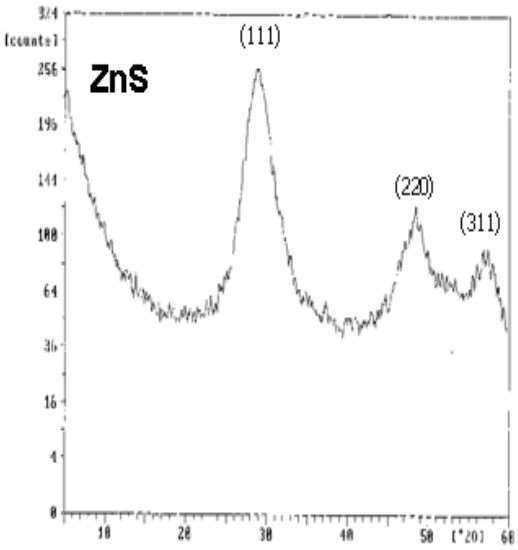

Fig. (1) XRD plot of n-ZnS at pH=12

Information of the strain and the particle size are obtained from the full width at half maximum (FWHMs) of the diffraction peaks. The FWHMs (β) can be expressed as a linear combination of the contributions from the strain (ε) and particle size (L) through the following relation [14]

$$\frac{\beta\cos\theta}{\lambda} = \frac{1}{L} + \frac{\varepsilon\sin\theta}{\lambda} \qquad (1)$$

Fig. (2) shows the plot of ($\beta\cos\theta$)/λ versus (sin θ)/λ for n-ZnS film at (pH = 12) which is a straight line. The reciprocal of intercept on the ($\beta\cos\theta$)/λ axis gives the average particle size as ~ 4 nm. The particle size increases (4.6 nm and 5.4 nm) as the pH value decreases from 12 to 10 and 7 respectively.

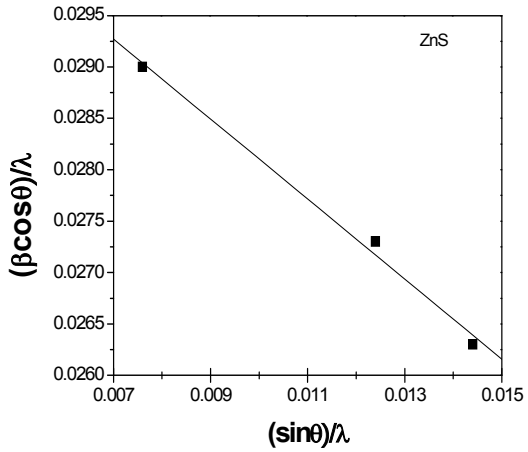

Fig. (2) Plot between ((βcosθ)/λ *vs.* (sin θ)/λ for n-ZnS film at pH=12

Fig. (3) shows the IR spectrum of n-ZnS film deposited at the KBr pallet. The presence of the band in the spectrum at 714cm^{-1} confirms the formation of ZnS. Further bands at 1396cm^{-1} and 1560cm^{-1} confirms the presence of capping agent trisodiumcitrate used for above study. The former band can be assigned to symmetric stretching of COO^-, while the later band can be assigned to the asymmetric COO^- [15]. Another band at 3322cm^{-1} can be assigned to OH stretching of trisodium citrate. The presence of the above mentioned bands indicate that trisodium citrate is bounded to the ZnS nanocrystals and it is arresting the growth of bulk crystals of ZnS.

Optical properties are studied by recording the transmission spectra of the films. Fig. (4) shows the transmission data of n-ZnS thin films deposited at different pH. The value of refractive index has been calculated using the relation [16]:

$$n = [\{2n_S\,(1\text{-}T)^{1/2} + n_S\,(2\text{-}T)\}/T]^{1/2} \qquad (2)$$

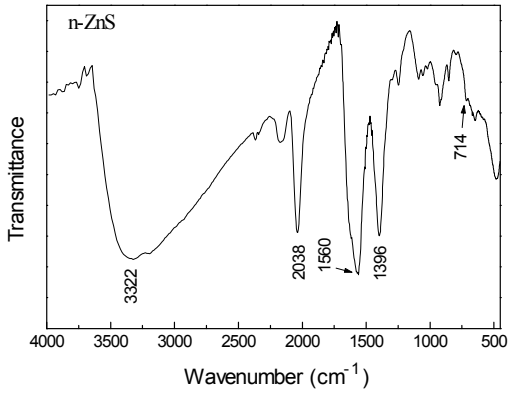

Fig. (3) IR spectrum of n-ZnS in wavenumber region 4000-450 cm^{-1}

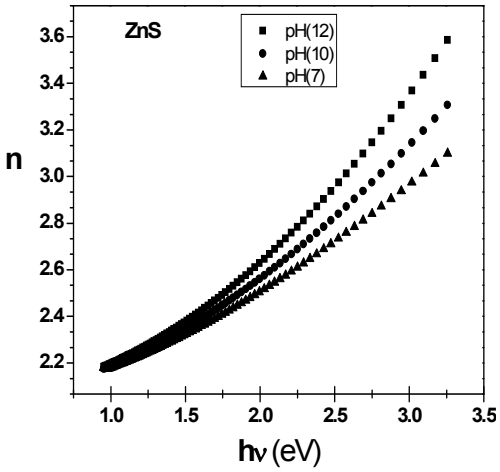

Fig. (4) Transmission curve of n-ZnS thin films

Fig. (5) shows the plots of refractive index (n) *vs.* $h\upsilon$ for all three thin films deposited at different pH values of the bath solution. It is clear from the figure that the value of n increases as the value of hυ increases. It is also clear from these plots that the value of n increases as the value of pH increases (as the particle size decreases). This increase in the value of n may be due to the quantum confinement effect due to the decrease in the particle size.

From the transmission data (see Fig. 4), nearly at the fundamental absorption edge, the values of absorption coefficient (α), are calculated in the region of strong absorption using the relation

$$\alpha = \frac{1}{d}\ln\left(\frac{1}{T}\right) \qquad (3)$$

The fundamental absorption, which corresponds to the transition from valence band to conduction band, can be used to determine the band gap of the material. The relation between α and the incident photon energy ($h\nu$) can be written as [17]

$$\alpha = \frac{A\left(h\nu - E_g\right)^n}{h\nu} \qquad (4)$$

where A is a constant, E_g is the band gap of the material and the exponent n depends on the type of transition

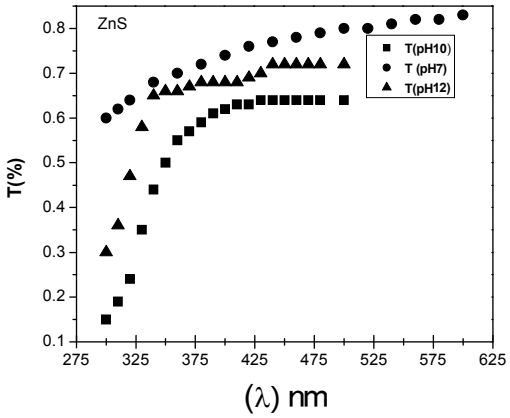

Fig. (5) Plots between *n* vs. *hν*

The n may have values 1/2, 2, 3/2 and 3 corresponding to the allowed direct, allowed indirect, forbidden direct and forbidden indirect transitions, respectively.

The value of optical gap is calculated by extrapolating the straight line portion of $(\alpha h\nu)^{1/n}$ vs $h\nu$ graph to $h\nu$ axis taking n = 0.5. Fig. (6) shows the plots of $(\alpha h\nu)^2$ vs $h\nu$ for the films deposited at different pH values.

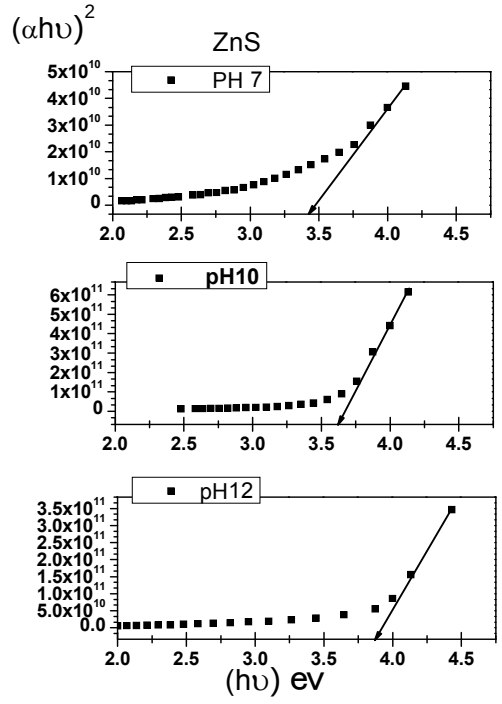

Fig. (6) Plots of $(\alpha h\nu)^2$ vs. $h\nu$ at different pH

The correct values of the optical gap calculated from the figure are (3.40 ± 0.01) eV, (3.68 ± 0.01) eV and (3.80 ± 0.01) eV for the films deposited at different pH i.e. 7, 10 and 12 respectively. The value of optical gap is found to decrease with the increase in the pH value. These

values of optical gap are inserted in Table 1. Clearly, the observed values of E_g are higher than the value of bulk optical gap of n-ZnS [(3.3±0.01) eV] [18] due to quantum confinement in the n-ZnS nanocrystallites.

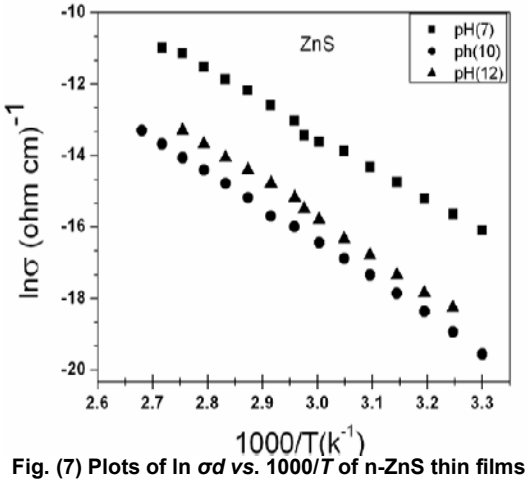

Fig. (7) Plots of ln *σd vs.* 1000/*T* of n-ZnS thin films at different pH

Table (1) The electrical and optical parameters of n-ZnS powder

pH	E_g (eV) (± 0.01)	Particle size (nm)	σ_d ($\Omega^{-1}cm^{-1}$)	E_a (eV) (± 0.01)
12	3.80	4.0	$(1.9 \pm 0.02)\times10^{-8}$	0.87
10	3.68	4.6	$(1.6 \pm 0.02)\times10^{-7}$	0.80
7	3.40	5.4	$(5.7 \pm 0.02)\times10^{-6}$	0.76

3.2 Electrical Properties

Fig. (7) shows the temperature dependence of dark conductivity (σ_d) of n-ZnS thin films deposited at different pH (12, 10 and 7). The electrical conductivity shows typical Arrhenius type of activation

$$\sigma_d = \sigma_o \exp\left(\frac{-\Delta E}{kT}\right) \quad (5)$$

where ΔE is the activation energy for dc conduction and k is the Boltzmann's constant.

The values of σ_d, calculated using Eq. (6), are $(1.9\pm0.02)\times10^{-8}$ $\Omega^{-1}cm^{-1}$, $(1.6\pm0.02)\times10^{-7}$ $\Omega^{-1}cm^{-1}$ and $(5.7\pm0.02)\times10^{-6}$ $\Omega^{-1}cm^{-1}$ for the films deposited at different pH values 12, 10 and 7 respectively. The value of σ_d increases as the particle size of n-ZnS increases. The increase in electrical conductivity and decrease in the activation energies as the value of pH decreases may be due to the change in structural parameters, improvement in crystallite and grain size, decrease in inter-crystallite boundaries (grain boundary domains) and removal of some impurities (adsorbed and absorbed gases).

4. Conclusions

n-ZnS powder as well as thin films have been deposited at different pH values of the deposition bath solution. These films have been deposited at different substrates. The particle size has been calculated using XRD data and found to be 4-6 nm. FTIR data confirm the formation of ZnS nanoparticles. The optical band gap has been calculated using optical data and it is found that the band gap increases as the pH value increases which is due to the quantum confinement effect. Electrical conductivity measurements have been done and it is found that the dark conductivity increases and dark activation energy decreases as the particle size increases.

Acknowledgements

This work is financially supported by CSIR (Major Research Project), New Delhi.

References

[1] A.P. Alivisatos, *Science*, 271 (1996) 933.
[2] G.Z. Wang et al., *Inorg. Chem. Commun.*, 4 (2001) 208.
[3] L.E. Brus, *Appl. Phys. A*, 53 (1991) 465.
[4] R. Maity and K.K. Chattopadhyay, *Nanotechnology*, 15 (2004) 812.
[5] S. Neeleshwar et al., *Phys. Rev. B*, 71 (2005) 201307(R).
[6] S. Coe et al., *Nature*, 420 (2002) 800.
[7] M.C. Beard, G.M. Turner, C.A. Schmuttenmaer, *Nano Lett.*, 2 (2002) 983.
[8] R.P. Raffaelle et al., *Prog. Photovoltaics*, 10 (2002) 433.
[9] V.I. Klimov et al., *Science,* 290 (2000) 314.
[10] A.P. Alivisatos, *Mater. Res. Soc. Bull.*, 23 (1998) 18.
[11] B. Zhang, J. Mu and D. Wang, *J. Dispersion Sci. & Technol.*, 26 (2005) 521.
[12] JCPDS Data File No. 8-459.
[13] JCPDS Data File No. 19-191.
[14] S.B. Qadri et al., *Phys. Rev. B*, 60 (1999) 9191.
[15] X. Zou, E. Ying and S. Dong, *Nanotechnology*, 17 (2006) 4758.
[16] J.C. Manifacier, J. Gasiot and J.P. Fillard, *Thin Solid Films*, 77 (1981) 67.
[17] J.I. Pankove, **"Optical Processes in Semiconductors"**, Englewood Cliffs. NJ: Prentice-Hall (1971).
[18] X. Zhong et al., *J. Mater. Chem.*, 14 (2004) 2790.

This article was reviewed at School of Applied Sciences, University of Technology, Baghdad, Iraq

(3-5) μm and (8-12) μm Wavelengths Ultra-Short Tunable Laser Pulses Using Optical Parametric Oscillation Technique

Anwaar A. Al- Dergazly[1]
Fareed F. Rasheed[2]
Sabah. M. Jumaa[3]

[1] Department of Laser and Optoelectronics Engineering, Alnahrain University, Baghdad, IRAQ
[2] Department of Laser and Optoelectronics Engineering, University of Technology, Baghdad, IRAQ
[3] Department of Physics, College of Science, Alnahrain University, Baghdad, IRAQ

A computational investigation has been carried out on optical parametric oscillation (OPO) technique. Non-collinear phase matching between the pumping wave and the two generated signal and idler waves has been taken into consideration. In order to separate the two generated waves a design has been put forward for a resonator for each wave within the same cavity and interrelated by mirror that transmits the pumped laser beam. The cavity configuration takes into account the three types of phase matching between the three waves. Solid state lasers were considered for pumping the nonlinear crystal. Furthermore, attention has been paid on the solid state Er:YAG laser for pumping the positive uniaxial $AgGaSe_2$ crystal to generate a signal wave of (8-12)μm wavelength so the generated idler wave from 3.82 to 4.55μm wavelength.

Keywords: OPO, Tunable lasers, Ultra-short pulses, Phase matching
Received: 20 July 2008, Revised: 9 October 2008, Accepted: 16 October 2008

1. Introduction

The infrared band is divided into four regions, short wavelength IR (SWIR) (1-3)μm, mid wavelength IR (MWIR) (3-5)μm, long wavelength IR (LWIR) (8-14)μm and very long wavelength IR (VLWIR) (14-24)μm spectral regions. Infrared technology has developed to a full-grown science, especially pushed by the explosive development of modern electronics and new detector materials' development. The result is that high performance IR imaging systems and, range finder utilizing both (3-5)μm and (8-12)μm wavelengths has become available, due to the atmospheric effect. The bands of wavelength in the region (3-5)μm and (8-12)μm can be generated by using OPO technique. Ultra-short light pulses have played an important role in quantum electronics research. The potential that optical bandwidth provide for ultrahigh speed scientific measurement, communication, and signal processing.

An OPO that will be studied in the present work is schematically represented by a nonlinear crystal within an optical cavity. When the nonlinear crystal is pumped it provides gain at two different frequencies (signal and idler). When the gain overcomes the loss the device reaches threshold and oscillates. The OPO system described here provides a relatively easy to operate combination of high resolution and tunability in the infrared, visible, and ultraviolet that opens up some important areas in spectroscopy, and communication, that were previously.

2. Performance Modeling of OPO

The simple design was designed for parametric devices which described gain, threshold, phase matching and conservation efficiency as a function of device and input parameters. A parametric gain coefficient g for the amplification of the signal wave can be defined by [1-2]

$$g = \sqrt{\frac{8\pi^2 d_{eff}^2}{\lambda_s \lambda_i n_s n_i n_p \varepsilon_o c} I_p} \qquad (1)$$

where I_p is the pump intensity, d_{eff} is the effective nonlinear coefficient, g connects the characteristics of pump, signal and idler fields.

In each passage through the material the intensity gains by a factor of [3]:

$$G = \exp(g\ell) \qquad (2)$$

where ℓ is the crystal length.

For steady-state oscillation an amplifier must fulfill the oscillator condition. The intensity of the wave I, starting at point O, must be reproduced after a full round trip. All losses such

as absorption, scattering, and laser output must be fully compensated by the amplification [4].

The loss of the pump beam due to growth required to increase signal or idler power from the noise level P_n to the threshold level P_s is defined as [5]:

$$L_{growth} = \left(\frac{P_n}{P_s}\right)\exp\left(-\frac{\ell}{t_p c}\right) \qquad (3)$$

where the exponential term represents the round trip losses and t_p pulse duration

3. Suggested Cavity Design

Single Resonant OPO (SRO) is the most common configuration for the mirror and resonator design, it is good conversion efficiency, and frequency and power output stability. These advantages more than offset the disadvantage of increased threshold relative to the Double Resonant OPO (DRO). The mode depends on the non-collinear phase matching. For non-collinear phase matching the direction of generated the signal and idler waves make an angle θ and ϕ, respectively with the optical axis of the nonlinear crystal. Hence one may split the two waves and design an SRO for each signal and idler wave. This means using two single resonant OPO instead of the double resonant. Thus there is good conversion efficiency, and frequency and power output stability for each wave. Further separation between the signal wave and the idler wave can be done without using an appropriate spectral filter or optical dispersive elements as shown in Fig. (1).

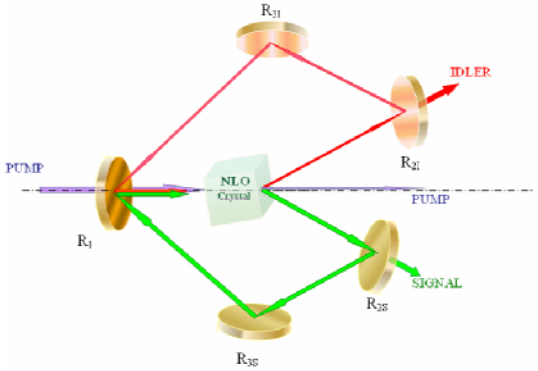

Fig. (1) Optical parametric oscillation cavity

Consider the propagation of light in the z-axis direction. The crystal in the OPO cavity is oriented at a polar angle θ_p. The first mirror R_1 should be 100% reflective to the signal and idler waves and 100% transmitting the pump wave. The second mirror R_2 reflects 90% of either signal or idler wave and transmits 100% the pump wave. The third mirror R_3 should be 100% reflective to either the signal or idler wave. The combination of mirrors R_2 and R_3 is needed for signal and idler resonators.

4. Computation Parts

4.1 Direction of Generated Waves Results

The crystal under consideration is the $AgGaSe_2$ crystal; it is a positive uniaxial crystal. Er:YAG laser is considered for use as a pumping source, thus the pumped wavelength is 2.9μm. The band of the signal wavelengths which will be generated is (8-12)μm; however, the band of the idler wavelengths that will be generated is (3.82-4.55)μm, which is within the region (3-5) μm atmospheric window.

At various pumping angles, the conversion efficiency of the crystal has been calculated for types 1 and 3 phase matching only because it found that the conversion efficiencies for types 1 and 2 in a positive uniaxial crystal are equal [6]. Phase matched polar and azimuthal angles for signal and idler waves have been calculated for the three types. At the pumping polar angle θ_p=22.5° there is no phase matching between the pump, signal, and idler waves if the signal wavelength varies between 10μm and 12μm; however, at wavelengths 8μm and 9μm there is phase matching in types 1 and 3, as shown in Fig. (2) and (3), respectively.

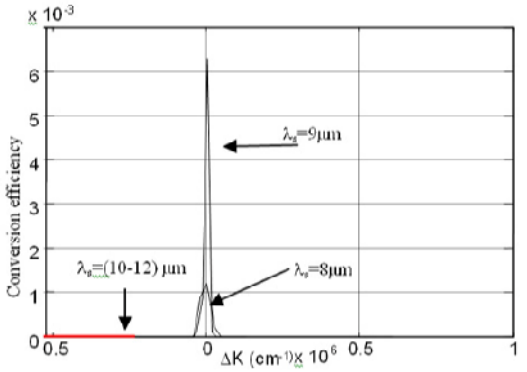

Fig. (2) Conversion efficiency versus ΔK for type 1 phase matching at θ_p=22.5° for (8-12)μm signal wavelength

The conversion efficiency of the 9um wavelength is higher than that for the 8μm wavelength for both types of phase matching. Furthermore, the conversion efficiency at type 1 phase matching is higher than that at type 3. Over the range of signal wavelengths under consideration, phase matching may occur as the pumping polar angle increases. Fig. (4) and (5) show that phase matching had occurred at θ_p=45°. Different values for the conversion efficiency have been obtained at different types of phase matching. At both types 1 and 3 phase matching the lowest conversion efficiency is found at λ_s=9μm and highest conversion efficiency at λ_s=12μm. However, type 1 gives rise to maximum conversion efficiency over the

whole range (8-12)μm of signal wavelength and (3.82-4.55)μm of idler wavelength.

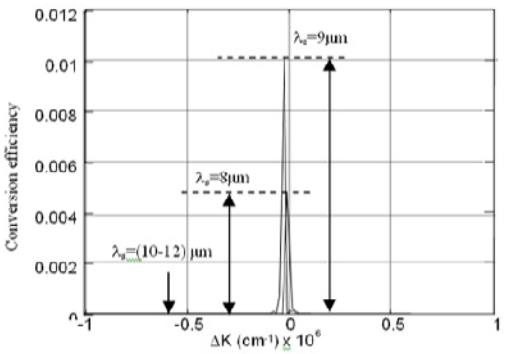

Fig. (3) Conversion versus ΔK for type 3 phase matching at θ_p=22.5° for (8-12)μm signal wavelength

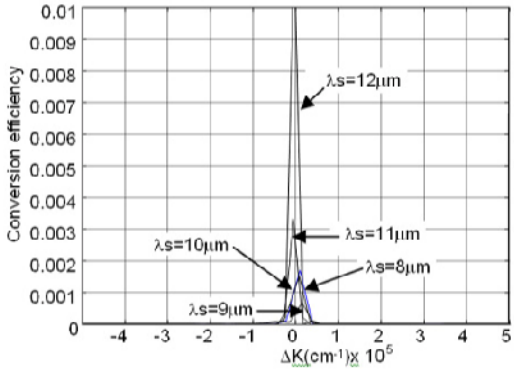

Fig. (4) Conversion efficiency versus ΔK for type 1 phase matching at θ_p=45° for (8-12)μm signal wavelength

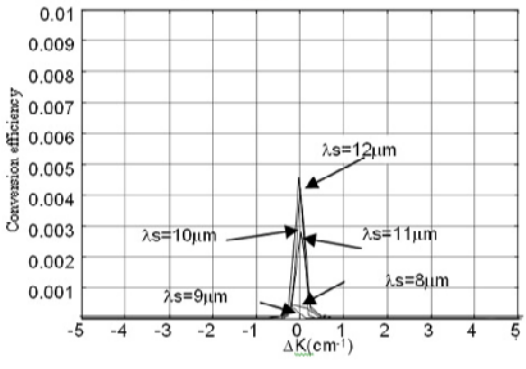

Fig. (5) Conversion efficiency versus ΔK for type 3 phase matching at θ_p=45° for (8-12)μm signal wavelength

At the three types of phase matching when θ_p=22.5°, the various angles of the signal and idler waves shown in figures (6-9) hold a linear relationship with the signal wavelength (λ_s) varying within the range (8-9)μm.

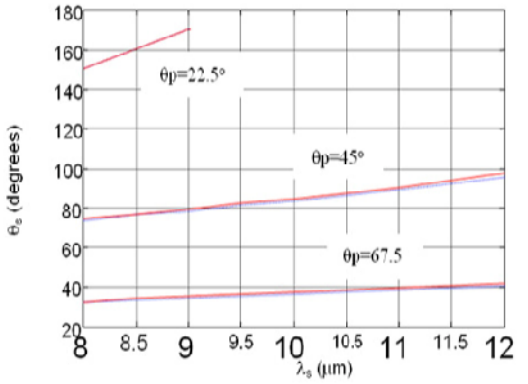

Fig. (6) Signal polar angle versus signal wavelength within the range (8-9)μm for types 1, 2 and 3 phase matching at different pumping polar angles

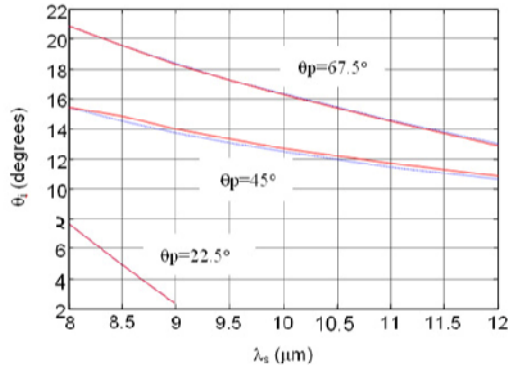

Fig. (7) Idler polar angle versus signal wavelength within the range (8-9)μm for types 1, 2 and 3 phase matching at different pumping polar angles

It is seen that the phase matching type has no effect on the variations of the various angles with λ_s. The above mentioned plots exhibit a positive gradient except that of the idler polar angle θ_i where the gradient is negative, i.e., θ_i decreases with increasing λ_s. In this case, the separation between the waves increases. Variation of the polar and azimuthal angles of the signal and idler waves with the signal wavelength over the range (8-12)μm at the three types of phase matching at θ_p>30° indicated that variations of θ_s, θ_i, ϕ_s and ϕ_i with λ_s are not affected at type 1 and 2 of phase matching. The effect of type 3 is a little different; it introduces a small constant difference as λ_s increases. It appears that increasing θ_p pushes the variations angles to vary in a more linear manner with λ_s irrespective of the phase matching type. The gradient of θ_s versus λ_s is positive whereas the graphs of θ_i, ϕ_s and ϕ_i versus λ_s have a negative gradient. Since θ_s increases and θ_i decreases with increasing λ_s, thus the separation between the signal and idler waves increases in the z-plane. As λ_s increases, ϕ_s increases in the $-xy$ plane and ϕ_i decreases in the xy plane; their separation is constant equals to π.

ISSN 1813-2065

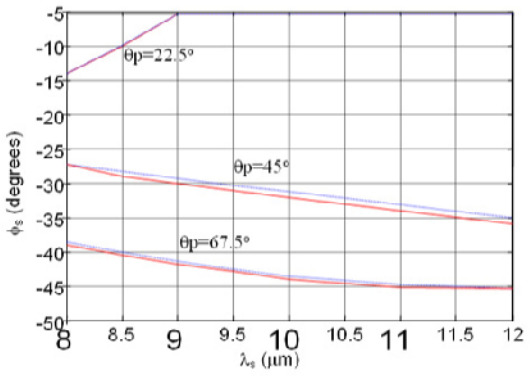

Fig. (8) Signal azimuthal angle versus signal wavelength within the range (8-9)μm for types 1, 2 and 3 phase matching at different pumping polar angles

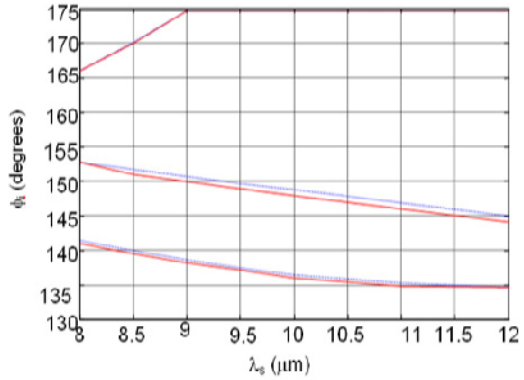

Fig. (9) Idler azimuthal angle versus signal wavelength within the range (8-9)μm for types 1, 2 and 3 phase matching at different pumping polar angles

4.2 The Properties of the Designed Cavity

The threshold pump intensity I_{th} is plotted in Fig. (10) as a function of signal wavelength λ_s at three types of phase matching are equals.

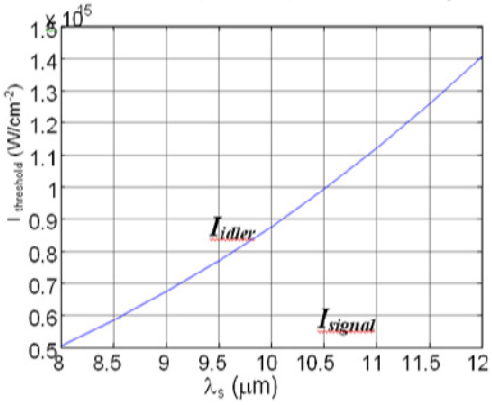

Fig. (10) Variation of threshold pump wave intensity with signal wavelengths at 45° polar pump angle

The figure suggests that the λ_s has a considerable effect on the threshold intensity. I_{th} reaches a minimum value of $0.5x10^{15}W/cm^2$ at λ_s=8μm; it then increasing when λ_s increase. I_{th} has a highest value of $1.4x10^{15}W/cm^2$ at λ_s=12μm. The intensity of the signal wave are constant for the wavelength region (8-12)μm at $3.2x10^{15}W/cm^{-2}$ and idler wave were increased when the signal wavelength increased this is for pump intensity equal $10x10^{16}W/cm^2$, as shown in Fig. (11).

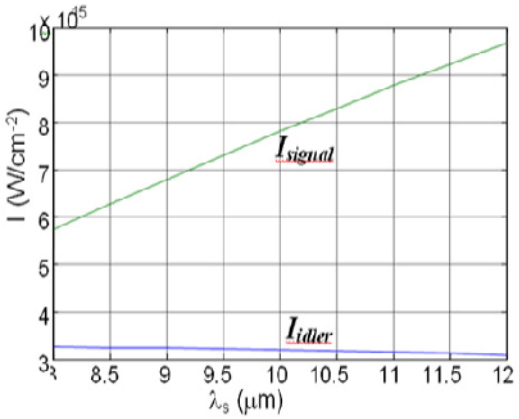

Fig. (11) Variation of signal and idler wave intensity with signal wavelengths at 45° polar pump angle

The intensity of the idler wave is higher than that for signal wave. The maximum rise time was obtained when the pumped pulse duration in nanometer is 0.29μs at λ_s from 10.5μm to 11μm, i.e., longer wave. The shorter wave is 2.79μs at λ_s=8μm, as shown in Fig. (12).

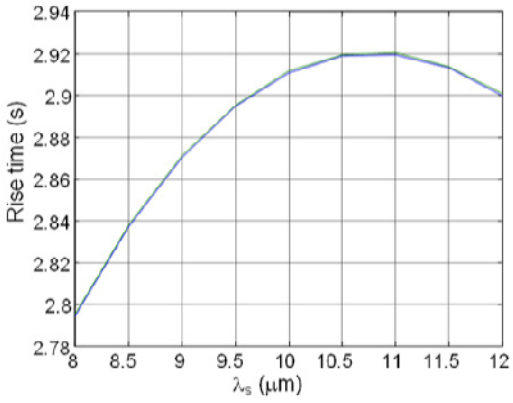

Fig. (12) Variation of signal and idler wave rise time with signal wavelengths at 45° polar pump angle

5. Conclusions

In the optical parametric oscillator system, consisting of a nonlinear crystal inserted in an optical resonator and pumped by an external laser source it appears that, the generated signal and idler waves from the cavity depend on many crucial factors. The type of laser source used to pump the nonlinear crystal with regarded to its intensity, wavelength and pulse duration highly affect the system. The intensity affects the generation of optical parametric oscillation; it must be within the range of the threshold

intensity for obtaining optical parametric oscillation and just below the intensity that would damage the nonlinear crystal. Both the wavelength and the direction of the pumped laser source affect the wavelengths and the directions of the generated signal and idler waves since the index of refraction depends on the wavelength and direction of propagation. The pulse duration of the pumped laser has its effect on the rise time and the pulse duration of the generated waves.

In non-collinear phase matching there is a difference in the direction of the generated waves. Therefore, the separation between the signal and idler waves can be done (without using appropriate filters or optical dispersive elements) by introducing a single resonant for each signal and idler wave in the same cavity. The cavity in this case will be more stable and have good conversion frequency for both the signal and idler waves.

Infrared technology has developed by using OPO technology. OPO can be used to generate band of wavelength in the region (3-5)μm and (8-12)μm. The conversion efficiency of the nonlinear crystals differs for different generated wavelength at each pumping angles. If the crystal was oriented in different angles, maximum conversion efficiency can be obtained for each generated wavelength at different types of phase matching.

References

[1] O. Aytür and Y. Dikmelik, *IEEE J.Quantum Electron.*, 34 (1998) 447-458.

[2] F. Zernike and J. Midwinter, **"Applied Nonlinear Optics"**, John-Wiley & Sons (1973).

[3] J. Rerdeyen, **"Laser Electronics"**, Prentice Hall (1981) 627-658.

[4] S. Schiller and J. Mlynek, *J. Opt. Soc. Am. B*, 16 (1999) 1819-1823.

[5] M. Padgett, *"Notes* **for** *Modern and Nonlinear Optics*", Department of Physics and Astronomy, University of Glasgow, Scotland (2005) 149-177.

[6] Anwaar A. Al-Dergazly, Ph.D. thesis, Al-Nahrain University (2005) 116-138.

[7] A. Yariv and P. Yah, **"Optical Waves in Crystal"**, John-Wiley & Sons (1984) 90-127.

[8] D. Roberts, *IEEE J. Quantum Electron.*, 28 (1992) 2058-2074.

[9] W. Koechner, **"Solid State Laser Engineering"**, 5th ed., Springer (1999) 587-624.

[10] R. Menzel, **"Photonics"**, Springer (2001) 30-49.

This article was reviewed at Department of Physics, Nizwa University, OMAN, and School of Applied Sciences, University of Technology, Baghdad, IRAQ

ISSN 1813-2065

Iraqi Journal of Applied Physics
Subject Index 2005-2008

Semiconductors & Optoelectronics

Solid State Physics & Applications

* * *

* * *

ISSN 1813-2065

Iraqi Journal of Applied Physics
Author Index 2005-2008

ISSN 1813-2065

IRAQI JOURNAL OF APPLIED PHYSICS

" INSTRUCTIONS TO AUTHORS "

A new Iraqi specialized quarterly periodical dedicated to publishing original papers, letters and reviews in:

Applied & Nonlinear Optics	Electronic Materials & Devices	Quantum Physics & Spectroscopy
Applied Mechanics & Thermodynamics	Laser Physics & Applications	Semiconductors & Optoelectronics
Digital & Optical Communications	Plasma Physics & Applications	Solid State Physics & Applications

CONTRIBUTIONS

Contributions to be published in this journal should be original research works, i.e., those not already published or submitted for publication elsewhere, individual papers or letters to editor.

SUBMISSION OF MANUSCRIPTS

Manuscripts should be submitted to the editor at the mailing address:

Iraqi Journal of Applied Physics
Editor-In-Chief
P. O. Box 55259, Baghdad 12001, IRAQ
editorinchief@ijap.org
irq_appl_phys@yahoo.com

Iraqi Journal of Applied Physics
Managing Editor
P. O. Box 55259, Baghdad 12001, IRAQ
editor@ijap.org
editor_ijap@yahoo.co.uk

MANUSCRIPTS

Two copies with soft copy on a compact disc (CD) should be submitted to Editor in the following configuration:

- Double-spaced one-side A4 size with 2.5 cm margins of all sides
- 12pt Times New Roman font
- Letters should not exceed 5 pages, papers no more 20 pages and reviews are up to author.
- Manuscripts presented in English only are accepted.
- Authors confirm affiliations, addresses and emails. Email is necessary for correspondences.
- English abstract not exceed 150 words
- 4 keywords (at least) should be maintained on (PACS preferred)
- Author(s) should express all quantities in SI units
- Equations should be written in equation form (italic and symbolic)
- Figures and Tables should be separated from text
- Figures and diagrams can be submitted in colors for assessment and they will be returned to authors after provide printable copies
- Charts should be indicated by the software used for
- Only original or high-resolution scanner photos are accepted
- References should be written in titles, full-name authors, names of publications, years, volumes, issues and pages (from-to)

PROOFS

Authors will receive proofs of papers and are requested to return one corrected hard copy with a WORD copy on a compact disc (CD). New materials inserted in the original text without Editor permission may cause rejection of paper.

COPYRIGHT FORM

Author(s) will be asked to transfer copyrights of the article to the Journal soon after acceptance of it. This will ensure the widest possible dissemination of information.

OFFPRINTS

Authors will receive offprints free of charge and any additional offprints can be ordered.

SUBSCRIPTION AND ORDERS

Annual fees (4 issues per year) of subscription are:

- 50 000 Iraqi dinars for individuals inside Iraq.
- 100 000 Iraqi dinars for establishments inside Iraq.
- 50 US$ for individuals abroad.
- 100 US$ for establishments abroad.

Fees are reduced by 25% for I.S.A.R.E.S.T. members. Orders of issues can be submitted by contacting the editor-in-chief or editorial secretary to maintain the address of issue delivery and payment way.

THE IRAQI JOURNAL OF APPLIED PHYSICS
EDITORIAL BOARD

COPYRIGHY RELEASE

Iraqi Journal of Applied Physics (IJAP)

We, the undersigned, the author/authors of the article titled

……
……
……
……
……
……

that is presented to the Iraqi Journal of Applied Physics (IJAP) for publication, declare that we have neither taken part or full text from any published work by others, nor presented or published it elsewhere in any other journal. We also declare transferring copyrights and conduct of this article to the Iraqi Journal of Applied Physics (IJAP) after accepting it for publication.

The authors will keep the following rights:

1. **Possession of the article such as patent rights.**
2. **Free of charge use of the article or part of it in any future work by the authors such as books and lecture notes without referring to the IJAP.**
3. **Republishing the article for any personal purposes of the authors after taking journal permission.**

To be signed by all authors:

Signature:……..date: ……..

Printed name: ……

Signature:……..date: ……..

Printed name: ……..

Signature:……..date: ……..

Printed name: ……..

Correspondence address:

……
……
……
Address:……
……
……
Telephone:……..email: ……..

Note: Please complete and sign this form and mail it to the below address with your manuscript

The Iraqi Journal of Applied Physics,
P. O. Box 55259, Baghdad 12001, IRAQ
Website: www.ijap.org, Email: editor@ijap.org, editor_ijap@yahoo.co.uk,
Tel.: +964-7901274190

 ISSN 1813-2065

IRAQI JOURNAL OF APPLIED PHYSICS

CONTENTS